KeA1

CHINESE ROOTS
GLOBAL IMPACT

Contents lists available at ScienceDirect

Petroleum Science

journal homepage: www.keaipublishing.com/en/journals/petroleum-science



Original Paper

A dual-scale failure evaluation method for Carbon-glass hybrid Fiber sucker rod and their joints under complex loads



Xiao-Xiao Lv a, c, Wen-Rui Jin b, *, Xin Zhang c

- ^a Postdoctoral Station of Mechanical Engineering, Tongji University, Shanghai, 201804, China
- ^b Sino-German College of Applied Sciences, Tongji University, Shanghai, 201804, China
- ^c National Engineering Research Center of Marine Geophysical Prospecting and Exploration and Development Equipment, China University of Petroleum, Qingdao, 266580, Shandong, China

ARTICLE INFO

Article history: Received 25 August 2024 Received in revised form 14 November 2024 Accepted 20 April 2025 Available online 22 April 2025

Edited by Teng Zhu

Keywords: Carbon-glass hybrid fiber sucker rod Dual-scale analysis Composite material failure Design of sucker rod

ABSTRACT

A hybrid fiber-reinforced polymer (HFRP) continuous sucker rod, comprising a carbon fiber-reinforced polymer (CFRP) core layer, a glass fiber-reinforced polymer (GFRP) winding layer, and a GFRP coating layer (CFRP:GFRP = 2:3), has been developed and widely used in oilfield extraction due to its lower specific gravity, enhanced corrosion resistance, and superior strength. However, HFRP rod joints and their adjacent sections are prone to multi-mode failures, including fracture, debonding, and cracking. Due to the complexity of joint structure and the coupling of tension, bending, and torsion, the failure mechanism is unclear. To address this issue, a dual-scale failure assessment methodology for HFRP rods was proposed, utilizing both macro and meso finite element models (FEM). This methodology was validated through tensile and bending experiments, which yielded critical loads for the ϕ 22 mm HFRP rod: a tensile load of 340.2 kN, a torque of 132.3 N m, and a bending moment of 1192.4 N m. Additionally, a comprehensive FEM of the joint was established, which identified potential failure points at the necking of the rotary joint, resin adhesive and the HFRP rod cross-section at the first groove tip. These failure modes closely matched the experimental observations. Furthermore, the simulation results show that stress concentration at the joint reduced the tensile, bending, and torsional strengths of the HFRP rod to 61%, 12%, and 82% of their original values, respectively. The effects of bending moments and torque on the tensile strength of HFRP rods were subsequently explored, leading to the development of an equivalent fatigue assessment method for HFRP rod joints. This method, based on the fatigue characteristics of HFRP rods and joint components, reveals that the primary cause of joint failure is the susceptibility of both the joint and the HFRP rod to bending moments and torque induced by dynamic buckling of the sucker rod string (SRS), Using this method, the fatigue ultimate axial force of the ω 22 mm HFRP joint was determined to be 91.5 kN, with corresponding fatigue ultimate torque and bending moment under an axial force of 62.4 kN being 89.3 N m and 71.5 N m, respectively. Finally, a design method incorporating a concentrated weighting strategy for HFRP-steel mixed rods was proposed to enhance their service life, and its effectiveness was demonstrated through on-site testing.

© 2025 The Authors. Publishing services by Elsevier B.V. on behalf of KeAi Communications Co. Ltd. This is an open access article under the CC BY-NC-ND license (http://creativecommons.org/licenses/by-nc-nd/

4.0/).

1. Introduction

Despite the gradual development and implementation of clean energy sources such as solar, wind, and hydrogen energy in industrial production and daily life to mitigate carbon emissions and protect the environment (Ji et al., 2022; Li et al., 2022), fossil fuels

* Corresponding author. E-mail address: wrjin@tongji.edu.cn (W.-R. Jin). continue to account for over 80% of global energy consumption (Meng et al., 2020). Consequently, the development of secure and efficient technologies for oil production remains a critical global issue. The sucker rod pumping system (SRPS) illustrated in Fig. 1 is a traditional artificial lifting method but still occupies a dominant position in the petroleum extraction industry (Jiang et al., 2024). In response to the challenges arising from the rapid increase of deep and corrosive wells in the middle to late stages of global oil field development (Lei et al., 2021; Elgaddafi et al., 2021; Zhang et al., 2024a), fiber-reinforced polymer composite sucker rods were

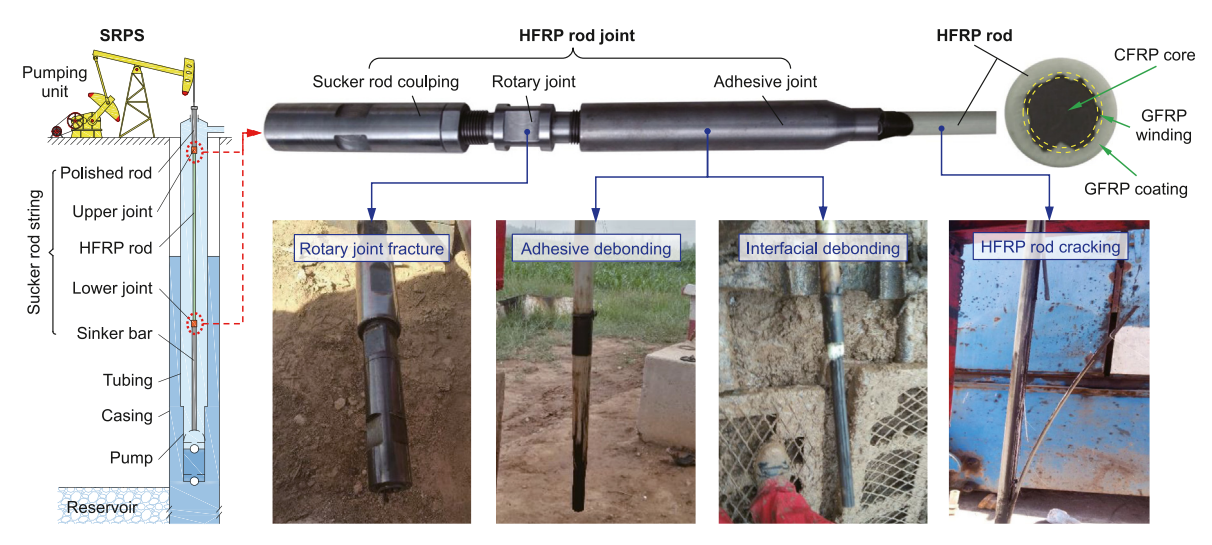


Fig. 1. Failure modes of HFRP rod joints.

developed and widely used (Zhang et al., 2023a; Guo et al., 2022a).

To eliminate the disadvantages of poor bending resistance of CFRP and low elastic modulus of GFRP, a carbon-glass HFRP suck rod was designed (Li et al., 2019a). Subsequently, research on fiber hybrid modes was conducted, resulting in two main modes: the shell-core mode, which has a simple and easy-to-control processing technology, and the random hybrid mode, which has better mechanical properties and fatigue resistance (Xian et al., 2021, 2022; Guo et al., 2022b; Zhang et al., 2024b, 2024c). Moreover, the bisphenol A epoxy resin is selected as the matrix to improve high-

temperature and corrosion resistance(Li et al., 2019b). Overall, the longitudinal tensile strength of HFRP rod is twice that of D-grade steel sucker rods, while its density is only 1/4 of steel. Although the cost of HFRP rods is 3~4 times that of D-grade sucker rods of the same specifications, HFRP rods can significantly reduce the load on the SRS. This allows for the use of smaller pumping units and motors, thereby reducing the one-time investment cost of oil extraction equipment (Lv et al., 2023).

Because of the flexibility of HFRP rods, a sinker bar is installed at

Nomenclati	ıre	T_{A}	torsion of the wellbore trajectory, m ⁻¹ ;
A_{Aj}	load stress transformation matrices for resin adhesive;	T_{CR}	stress conversion matrix between rectangular CS and cylindrical CS (appendix);
A_F	load-stress transformation coefficient matrix;	$T_{y\beta}$	stress transformation matrix corresponding to a rotation of the CS around the Y-axis by angle β (appendix);
A_{H}	cross-sectional area of the HFRP rod, m ² ;	T_{β}	off-axis stress transformation matrix (appendix).
A _s	cross-sectional area of the sinker bar, m ² ;	Greek symbo	
A_{Si}	load stress transformation matrices for the steel joint;	$[\sigma_{A}]$	allowable fatigue strength of the resin adhesive, Pa;
A_{σ}	stress amplification factor;	$[\sigma_{\rm S}]$	allowable fatigue stress of the steel joint, Pa;
В	width of unidirectional CFRP (GFRP) specimen, m;	β	lay angle, rad;
$c_i (i = 0,, 9)$) fitting coefficients of effect function;	δ_{A}	service factor;
$d_{\rm h}$	minimum diameter of a sinker bar that does not buckle, m;	ε	strain vector;
e, u, w	displacements of the sucker rod nodes along the tangential, normal,	ε_{C}	strain vector in cylindrical coordinates;
	and sub-normal directions, m;		
$E_{ m f}$	elastic modulus of fiber, Pa;	ζ_{A}	FSM of the resin adhesive;
$E_i(i = 1, 2, 3)$) elastic modulus in the <i>i</i> direction, Pa;	$\zeta_{\rm HI}$	FSM of the HFRP rods at the joints;
E_k	elastic modulus of the k-th stage sucker rod, Pa;	ζ_{HR}	FSM of the HFRP rods;
$E_{\rm m}$	elastic modulus of matrix, Pa;	ζ_{J}	FSM of the HFRP rod joints;
E_s	elastic modulus of sinker bar, Pa;	$\zeta_{\mathbf{M}}$	factor accounting for fiber reinforcement.
F	load vector;	ζ_{S}	FSM of the steel joint;
F_0	is maximum concentrated compressive load of SRS bottom, N;	η_{A}	strength margin of the HFRP rod;
F_{A}	axial force, N;	$\eta_{ m f}$	volume fractions of fiber;
$f_{A}(\cdot)$	mapping function from complex loads to strength margin;	$\eta_{\mathrm{F}i}$	strength margins of each meso critical point of fiber;
F_{AC-cr}	critical axial force of HFRP rod under the influence of bending moment and torque, N;	η_{Lk}	strength margin of macro critical point of the HFRP section;
F_{A-cr}	critical axial force of HFRP rod, N;	$\eta_{ m m}$	volume fractions of matrix;
F_{AJC-cr}	critical axial force of HFRP rod joint under the influence of bending moment and torque, N;	$\eta_{\mathrm{M}j}$	strength margins of each meso critical point of matrix;
$F_{\mathbf{b}}$	tensile ultimate load of CFRP (GFRP) specimen, N;	θ_{b}	deflection angle of SRS caused by buckling, rad;
F_{b-cr}	critical buckling load of SRS, N;	К	shear coefficient of Timoshenko;
$F_{\mathrm{B-cr}}$	ultimate bending load of HFRP rod, N;	$v_{ij} (i, j = 1, 2, 3, i \neq j)$	Poisson's ratio;
$F_{\mathrm{e} au}$, $F_{\mathrm{e}\mathrm{n}}$, $F_{\mathrm{e}\mathrm{b}}$	tangential, normal, sub-normal internal forces, N;	ρ_k	density of the k -th stage sucker rod, kg/m^3 ;
$f_{ m e au}, f_{ m en}, f_{ m eb}$	tangential, normal, sub-normal external forces, N/s;	ρ_s	density of sinker bar, kg/m³;
			(continued on next page)

(continued on next page)

(continued)

$F_i(i=x,y,z)$	components of concentrated force, N;	$\overline{\sigma}$	macro stress vectors, Pa;
f J TB (\cdot)	effect function for the tensile capacity of HFRP rods at joints;	$\widehat{m{\sigma}}$	meso stress vectors, Pa;
$fR TB(\cdot)$	effect function for the tensile capacity of HFRP rods;	σ	stress vector, Pa;
g	gravitational acceleration, m/s ² ;	σ_{-1}	fatigue strength of HFRP, Pa;
$G_{ij}(i, j = 1, 2, 3, i \neq j)$	shear elastic modulus in <i>i-j</i> planes, Pa;	σ_{-1E}	equivalent fatigue strength of HFRP, Pa;
G_k	shear modulus of the k-th stage sucker rod, Pa;	σ_{Aj}	stress vectors at potential failure points on resin adhesive, Pa;
G_s	shear modulus of steel sucker rod, Pa;	$\overline{\sigma}_{C}$	macro stress vector in cylindrical CS, Pa;
I_k	moment of inertia of the k -th stage sucker rod, m^4 ;	$\widehat{\sigma}_{f1}$	longitudinal meso normal stress of fiber, Pa;
I_s	moment of inertia of the sinker bar, m ⁴ ;	σ_{fl}	stress in the fiber along the fiber direction, Pa;
J_{1-cr}	critical first stress invariant, Pa;	$\sigma_{ m fc}$	compressive strength of the fiber, Pa;
$J_{i}(i = 1,2)$	i-st stress invariant of the matrix, Pa;	σ_{ft}	tensile strength of the fiber, Pa;
J_k	polar moment of inertia of the k-th stage sucker rod, m ⁴ ;	$\sigma_i(i = 1,2,3)$	normal stress component, Pa;
J_s	polar moment of inertia of sinker bar, m ⁴ ;	σmax VM-Si	maximum von Mises stresses at the potential failure points of the steel joint, Pa;
k_{A}	curvature of the wellbore trajectory, m ⁻¹ ;	$\sigma_{ m mc}$	compressive strengths of the resin matrix, Pa;
k _C	curvature of the sucker rod, m ⁻¹ ;	σmin VM-Si	minimum von Mises stresses at the potential failure points of the steel joint, Pa;
$L_{\rm B}$	bending span, m;	$\sigma_{ m mt}$	tensile strengths of the resin matrix, Pa;
$M_{\rm B}$	bending moment, N·m;	$\overline{\sigma}_{R}$	macro stress vector in rectangular CS, Pa;
$M_{\rm Ba}$	maximum additional bending moment, N·m;	$\sigma_{ m sb}$	ultimate strength of steel joint, Pa;
M _{B-cr}	critical bending moment of HFRP rod, N·m;	σ_{Si}	stress vectors at potential failure points on the steel joint,Pa;
M _{BI-cr}	critical bending moment of HFRP rod at joint, N·m;	$\sigma_{\rm UTS}$	longitudinal tensile strength of HFRP rod, Pa;
$M_i(i = f, m)$	engineering elastic constants of fiber or matrix;	$\sigma_{ m VM}$	von Mises stress of the matrix, Pa;
$M_i(j=x,y,z)$	components of moment, N·m;	$\sigma_{\text{VM-Ai}}$	von Mises stress at potential failure point on adhesive, Pa;
$M_{\rm T}$	torque, N·m;	$\sigma_{ m VM-cr}$	critical von Mises stress of the matrix, Pa;
M_{Ta}	maximum additional torque, N·m;	$\tau_{ii}(i, j = 1, 2,$	shear stress component, Pa;
1a	mammam additional corque, m,	$3, i \neq j$	Shear sucess component, ray
M_{T-cr}	critical torque of HFRP rod, N·m;	φ	torsional angle of the sucker rod, rad;
$M_{\rm TJ-cr}$	critical torque of HFRP rod at joint, N·m;	Abbreviation	
N_{f0}	specified fatigue cycle;	CFRP	carbon fiber reinforced polymer;
$p_{ m h}$	pitch of helical buckling, m;	CS	coordinate system;
PL_{Si}	cyclic stress ratio at potential failure point on the steel joint;	FATS	fiber axial tensile strength;
Q	stiffness matrix, Pa;	FEM	finite element models;
$\overline{\mathbf{Q}}$	off-axis stiffness matrix in cylindrical CS, Pa;	FSM	fatigue strength margin;
r_0	half of the difference between the tubing inner diameter and the diameter of the steel sucker rod, m;	GFRP	glass fiber reinforced polymer;
S	coordinate of the sucker rod node, m;	HFRP	hybrid fiber reinforced polymer;
S	stroke of the pumping unit, m;	MMF	Meso-Mechanics of Failure;
s_{w}	dynamic coordinates of the sucker rod node,m, $s_w = s + e(0,t)-S$;	RUC	repeated unit cell;
T	thickness of unidirectional CFRP (GFRP) specimen, m;	RVE	representative volume element;
t	time, s;	SEM	scanning electron microscopy;
$T_{1\psi}$	stress coordinate transformation matrix when rotating around axis		single-lap joint;
ıψ	1 by angle ψ (appendix);	,	○ 10 · ·
	J J / CIF " //	SRPS	sucker rod pumping system;
		SRS	sucker rod string;
			-

the lower end to ensure the smooth movement of the SRS during the downstroke. Consequently, adhesive joints are needed to connect the HFRP rods with the sinker bar and polished rod. These HFRP rod joints and adjacent rods are susceptible to multi-mode failure, as shown in Fig. 1, including fracture, debonding, and cracking, which severely affects the service life of SRS. Therefore, understanding the root causes of failure in HFRP rods and their joints is critically important.

Due to the extensive use of composite materials, significant research has focused on their failure mechanisms and adhesive failure. Microscopic techniques such as scanning electron microscopy (SEM) (Zhang et al., 2023b), and energy-dispersive X-ray spectroscopy are valuable for observing internal damage in fiber-reinforced polymers. However, these methods have limitations in capturing local damage in 3D complex structures. Therefore, multiscale theories (Qi et al., 2019; Liu et al., 2023) and computational simulation techniques (Noh et al., 2023; Zhang et al., 2024c; Feng et al., 2024) have gained increased attention.

The Tsai-Wu failure criterion (Tsai and Wu, 1971), based on deformation energy theory, was initially introduced, followed by the Hashin criterion (Hashin, 1987) which predicts crack location and propagation. Further improvements, such as the Chang and Chang criteria (Chang and Chang, 1987; Gu and Chen, 2017), consider shear stress effects on failure modes. Recent

advancements include the use of FEM with representative volume elements (RVEs) to predict stress distribution in complex composites. Van Dongen et al. (2018) proposed a mixed method for progressive damage analysis using the eXtended Finite Element Method and Cohesive Zone Model, verified by open hole tensile tests. To elucidate the thermal aging mechanisms in CFRP composite, Cao et al. (2023) developed a multi-scale model predicting damage evolution under thermal oxidation. Yuan et al. (2022) adopted a 2D RVE to study out-of-plane shear loads on cross-laminated plates. Shi et al. (2024) introduced a novel cross-scale approach to map macro/meso-layer behavior in the complex resin-fiber-interface. Xian et al. (2024) experimentally determined the failure mode of glass fiber reinforced polypropylene in corrosive solutions.

For easily measurable properties, such as compressive and tensile strength, indoor experimental methods remain the most effective (Rodsin et al., 2022; Mushtaq et al., 2022). For HFRP sucker rod body, some scholars have conducted experimental tests on the tensile-tensile fatigue, interfacial shear, bending and other properties under specific environments, and obtained the damage mechanism under single loads (Li et al., 2018; Li et, al., 2019b; Li et al., 2020a; Guo et al., 2021; Guo et al., 2022a). However, due to experimental equipment limitations, testing the performance of HFRP rods under complex loads remains challenging.

Regarding adhesive bond failure, Kim et al. (2008) introduced a novel methodology for predicting failure in single-lap joints (SLIs) by considering both adherent and adhesive failure, and developed a new strength enhancement approach. Hou et al. (2022) employed a multi-scale modeling method to elucidate the mechanical behavior of SLIs and double-lap joints for plain woven composite under tensile load. Subsequently, leveraging these methodologies, the impact of bonding structure parameters, including overlap length. adherent thickness, adhesive stiffness, adherent bending stiffness, and fiber orientation sequences, on SLI performance was analyzed (Reis et al., 2011; Ozel et al., 2014; Hasheminia et al., 2019; Wang et al., 2021). Ke et al. (2024) investigated the performance evolution of epoxy adhesives and CFRP-steel epoxy-bonded joints after hygrothermal exposure through experiments. Wang and Xian (2021b) found through experimental research that differences in the coefficient of thermal expansion significantly weaken the bond strength between CFRP and steel. To assess the bonded performance under complex operational conditions, an energy-based fatigue life prediction model was presented and improved, with enhancements through neural network technology enabling accurate prediction of multi-axial fatigue life (Hafiz et al., 2013; Wu et al., 2021; Zhang et al., 2022; Tanulia et al., 2022).

In summary, extensive analysis methods, strength prediction and influencing factors have been studied for the failure of composite materials and their joints. Most research, aimed at verification, has focused on sheet-like composite materials and single joints. However, HFRP sucker rods are cylindrical materials with complex internal structures. While Li et al. (2020b) proposed an innovative anchoring technique for HFRP rods and steel rods that offers high tensile performance, adhesive joints remain dominant in oilfield practices due to the complexity of new technology operations and their uncertainty regarding complex loads. These adhesive joints feature multiple wedge-shaped grooves for resin adhesive, further complicating the internal structure. Consequently, the mechanical properties and failure mechanisms of HFRP rods and their joints under the complex loading conditions in oil well operations remain unclear, significantly hindering the optimization of mixed SRS and the full utilization of HFRP rod performance.

Based on the above analysis, this paper proposes a dual-scale failure evaluation method and an equivalent fatigue failure assessment method to reveal the root causes of the HFRP rod and joint failures. The main contributions of this paper can be summed as fourfold. (1) A dual-scale failure assessment methodology for HFRP rods was proposed, incorporating meso-scale RVE of fibers and matrix, and multi-layer macro-scale FEM of the rod structure, which was verified through tensile and bending tests. (2) A threedimensional comprehensive FEM of the HFRP rod joint was established, quantifying the impact of stress concentration at the joint on the mechanical properties of HFRP rods. (3) An equivalent fatigue failure assessment method for the HFRP rod joints subjected to complex loads was proposed for the first time, employing a dualscale failure criterion. (4) A design method incorporating a concentrated weighting strategy for HFRP-steel mixed rods was proposed to extend their service life, with effectiveness demonstrated through on-site testing.

2. Material parameters and failure modes of HFRP rod

2.1. Internal structure and parameters of HFRP rod

Taking HFRP rods with a shell-core hybrid mode as the research object, as shown in Fig. 1, the HFRP rod consists of a multi-layer composite structure (Li et al., 2020c; Guo et al., 2022c). The core is made of CFRP, which significantly enhances the rod's strength.

Surrounding this core is a GFRP winding layer, designed to prevent the dispersion of CFRP core. The outer coating layer, also made of GFRP, provides improved ductility and corrosion resistance (Li et al., 2020d). The intricate internal architecture of HFRP rod is detailed in Fig. 2(a), illustrating that the fibers within the CFRP core and the GFRP coating layers are aligned parallel to the rod's longitudinal axis, whereas the fibers within the winding layer are positioned at $\pm 45^{\circ}$ relative to this axis. The basic parameters of HFRP sucker rod are presented in Table 1.

Table 2 elucidates the fundamental material properties of carbon fibers, glass fibers, and the epoxy resin matrix utilized in the manufacturing process of HFRP rods. Notably, carbon fiber is polycrystalline and shows strong anisotropy, while glass fiber and epoxy resin are isotropic.

Before analyzing the mechanical properties of composite materials, it is essential to homogenize them. The HFRP rod consists of four layers of unidirectional fiber composites, and their mechanical properties can be examined using the unidirectional laminate model depicted in Fig. 2(b). Unidirectional laminates can be homogenized into anisotropic homogeneous materials, and the stress-strain relationship within these laminates, as defined in the coordinate system (CS) (1-2-3) aligned with the fiber directions, is given by:

$$\begin{bmatrix} \sigma_1 \\ \sigma_2 \\ \sigma_3 \\ \tau_{23} \\ \tau_{31} \\ \tau_{12} \end{bmatrix} = \begin{bmatrix} Q_{11} & Q_{12} & Q_{13} & 0 & 0 & 0 \\ Q_{12} & Q_{22} & Q_{23} & 0 & 0 & 0 \\ Q_{13} & Q_{23} & Q_{33} & 0 & 0 & 0 \\ 0 & 0 & 0 & Q_{44} & 0 & 0 \\ 0 & 0 & 0 & 0 & Q_{55} & 0 \\ 0 & 0 & 0 & 0 & 0 & Q_{66} \end{bmatrix} \begin{bmatrix} \varepsilon_1 \\ \varepsilon_2 \\ \varepsilon_3 \\ \gamma_{23} \\ \gamma_{31} \\ \gamma_{12} \end{bmatrix}$$
(1)

The above formula can be simplified to:

$$\sigma = \mathbf{Q}\varepsilon$$
 (2)

where \mathbf{Q} can be derived from the engineering elastic constants of composites, expressed as:

$$\begin{aligned} Q_{11} &= E_1 \frac{1 - \nu_{23} \nu_{32}}{\Lambda}, Q_{22} &= E_2 \frac{1 - \nu_{31} \nu_{13}}{\Lambda}, Q_{33} &= E_3 \frac{1 - \nu_{12} \nu_{21}}{\Lambda}, \\ Q_{44} &= \kappa G_{23}, Q_{55} &= \kappa G_{31}, Q_{66} &= G_{12} \\ Q_{12} &= E_1 \frac{\nu_{21} + \nu_{31} \nu_{23}}{\Lambda} &= E_2 \frac{\nu_{12} + \nu_{32} \nu_{13}}{\Lambda}, \\ Q_{13} &= E_1 \frac{\nu_{31} + \nu_{21} \nu_{32}}{\Lambda} &= E_3 \frac{\nu_{13} + \nu_{12} \nu_{23}}{\Lambda} \\ Q_{23} &= E_2 \frac{\nu_{32} + \nu_{12} \nu_{31}}{\Lambda} &= E_3 \frac{\nu_{23} + \nu_{21} \nu_{13}}{\Lambda}, \\ \Lambda &= 1 - \nu_{12} \nu_{21} - \nu_{23} \nu_{32} - \nu_{13} \nu_{31} - 2\nu_{21} \nu_{32} \nu_{13} \end{aligned}$$

$$(3)$$

The engineering elastic constants of single fiber composite laminates can be determined using the mixing law of composites.

$$\begin{cases} E_{1} = E_{f}\eta_{f} + E_{m}\eta_{m}, \nu_{12} = \nu_{f}\eta_{f} + \nu_{m}\eta_{m} \\ M = \frac{1 + \zeta_{M}\zeta_{1}\eta_{f}}{1 - \zeta_{1}\eta_{f}}M_{m}, \zeta_{1} = \frac{\left(M_{f}/M_{m}\right) - 1}{\left(M_{f}/M_{m}\right) + \zeta_{M}} \end{cases}$$
(4)

Based on the fibers-to-resin ratio in Table 1, the engineering elastic constants for CFRP and GFRP can be calculated using Eq. (3) and Eq. (4) as detailed in Table 3. The average deviation between these calculated values and the manufacturer's measured results is 5.0%, demonstrating that the computed engineering elastic constants are reliable for performance analysis of the HFRP rod.

Fig. 2(c) illustrates the cylindrical composite material in the

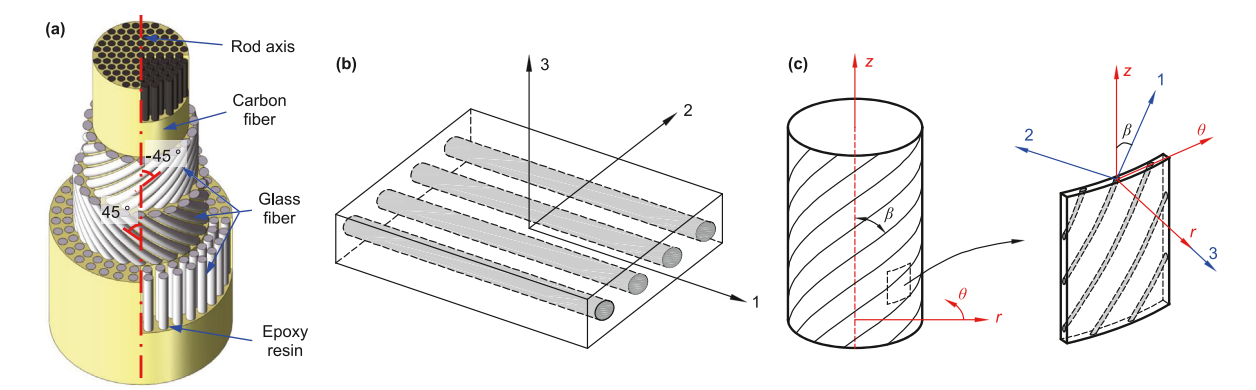


Fig. 2. HFRP rod structure and modeling. (a) Internal structure; (b) Composite unidirectional laminate; (c) Coordinate System for arbitrary layer of cylindrical composite materials.

Table 1Basic parameters of carbon rods.

Parameters	Value
Axial tensile strength, MPa	1560
Axial fatigue strength, MPa	479
Density, kg/m ³	2040
Volume ratio of fiber to resin	7:3
Volume ratio of CFRP to GFRP	2:3

cylindrical CS (r, θ, z) , where β denotes the ply angle, representing the angle between the fiber direction and the z-axis. The stress-strain relationship for each point in an elastic material within cylindrical coordinates can be expressed as:

$$\begin{cases}
\boldsymbol{\sigma}_{\mathsf{C}} = \overline{\mathbf{Q}}\boldsymbol{\varepsilon}_{\mathsf{C}} \\
\boldsymbol{\sigma}_{\mathsf{C}} = \begin{bmatrix} \sigma_{r} & \sigma_{\theta} & \sigma_{z} & \tau_{\theta z} & \tau_{z r} & \tau_{r \theta} \end{bmatrix}^{\mathsf{T}} \\
\boldsymbol{\varepsilon}_{\mathsf{C}} = \begin{bmatrix} \varepsilon_{r} & \varepsilon_{\theta} & \varepsilon_{z} & \gamma_{\theta z} & \gamma_{z r} & \gamma_{r \theta} \end{bmatrix}^{\mathsf{T}}
\end{cases} \tag{5}$$

where,

$\overline{\mathbf{Q}} = \mathbf{T}_{\beta}^{-1} \mathbf{Q} \mathbf{T}_{\beta}^{-\mathrm{T}}$	(6)
$\mathbf{Q} = \mathbf{T}_{\beta}^{-1} \mathbf{Q} \mathbf{T}_{\beta}^{-1}$	(6

Based on the structure of the HFRP rod, the lay angle of each layer is given by:

$$\beta = \begin{cases} 0 & \text{CFRP core and GFRP coating layer} \\ \pm 45^{\circ} & \text{GFRP winding layer} \end{cases}$$
 (7)

2.2. Characterization of microscopic failure modes

The failure mechanisms of HFRP rods can be categorized into fiber failure and matrix failure. When the composite is subjected to loading along the fiber direction (0°), the fibers primarily bear the load, leading to predominant fiber damage. Conversely, when the composite is loaded in other directions, matrix failure becomes more prominent due to the comparatively lower strength of the matrix

In this study, the Meso-Mechanics of Failure (MMF) framework (Ha et al., 2010) is adopted to evaluate the failure of both the fiber and the resin matrix. Within the MMF framework, the failure of fibers is assessed using the maximum longitudinal stress criterion:

Material parameters	mod	nsile Iulus, Pa	She modi GI	ılus,	Poisso	n's ratio	Density, kg⋅m ⁻³	Tensile strength, MPa	Compressive streng, MPa
T-300 Carbon fibre	E _{f1} E _{f2} E _{f3}	260 20 20	G_{f23} G_{f12} G_{f13}	29 6 6	ν _{f23} ν _{f12} ν _{f13}	0.32 0.3 0.3	1800	3680	3200
Glass fibre Epoxy resin		74 4	30 1.3			.22 .38	2550 1200	3430 87	2800 105

Table 3Comparison between calculated and measured engineering elastic constants of CFRP and GFRP.

Material parameters		Tensile m	odulus, GPa	Poisson's ratio		Shear modulus, GPa		Danaita, I.a. a3
Materia	i parameters	E_1	$E_2(E_3)$	$v_{12}(v_{13})$	ν_{23}	$G_{12}(G_{13})$	G ₂₃	Density, kg⋅m ⁻³
CFRP	Calculated	183	28.2	0.34	0.35	5.54	10.6	1620
	Measured	180	30	0.32	0.34	6	10	1650
	Error, %	2.3	6.0	6.3	2.9	7.6	6.0	1.8
GFRP	Calculated	53	21.8	0.27	0.29	2.12	8.6	2145
	Measured	52	20	0.28	0.3	2	9	2300
	Error, %	2.0	9.0	3.6	3.3	6.0	4.4	6.7

$$\begin{cases} \sigma_{f1} > \sigma_{ft} \rightarrow \text{Fiber tensile failure} \\ \sigma_{f1} \leq -\sigma_{fc} \rightarrow \text{Fiber compression failure} \end{cases}$$
 (8)

Matrix failure is evaluated using the following criterion:

$$\begin{cases} (J_{1}/J_{1-cr}) + (\sigma_{VM}/\sigma_{VM-cr})^{2} \ge 1 \rightarrow \text{Matrix failure} \\ J_{1} = \sigma_{1} + \sigma_{2} + \sigma_{3} \\ J_{2} = \sigma_{1}\sigma_{2} + \sigma_{1}\sigma_{3} + \sigma_{2}\sigma_{3} - \left(\tau_{12}^{2} + \tau_{13}^{2} + \tau_{23}^{2}\right) \\ \sigma_{VM} = \sqrt{J_{1}^{2} - 3J_{2}} \end{cases}$$
(9)

The tensile and compressive strengths of carbon and glass fibers are detailed in Table 2. The critical values for the resin matrix, σ_{VM-cr} and J_{1-cr} , are determined using Eq. (10) based on the tensile and compressive strengths of epoxy resin:

$$\begin{cases} \sigma_{VM-cr} = \sqrt{\sigma_{mt}\sigma_{mc}} \\ J_{1-cr} = \sigma_{mt}\sigma_{mc}/(\sigma_{mc} - \sigma_{mt}) \end{cases}$$
 (10)

Therefore, to assess the failure of HFRP rods using MMF, a dual-scale analysis is required to obtain the mesoscopic stresses in both the fiber and matrix.

3. Dual-scale failure evaluation method

In this section, firstly, a model for predicting the macroscopic loads on the SRS is established. Then, a macroscopic FEM for the HFRP rod, alongside a mesoscopic FEM for the fiber and resin matrix is built, which enables the detailed analysis of microscopic stresses within the fibers and resin matrix under applied macroscopic loads. Subsequently, by integrating the microscopic failure modes, a dual-scale methodology for evaluating failure in HFRP rods is presented. Finally, based on the dual scale method, an equivalent fatigue failure assessment method for HFRP rod joints is constructed.

3.1. Macro load model

To perform a failure evaluation of HFRP rods and joints, it is essential to predict the complex loading conditions that the SRS will encounter during operation. The axial force can be derived from the longitudinal vibration model (Sun et al., 2018; Lv et al., 2021). Meanwhile, the bending moment and torque on the sucker rod can be determined using the model developed by Wang et al. (2024) (refer to Eq. (11) and Eq. (12) for specifics, with boundary and initial conditions detailed in the referenced literature).

$$\begin{cases} \frac{\partial F_{e\tau}(s,t)}{\partial s} - F_{en}(s,t)k_{A}(s_{w}) + f_{e\tau}(s,t) = \rho_{k}A_{k}\frac{\partial^{2}e(s,t)}{\partial t^{2}} \\ F_{e\tau}(s,t)k_{A}(s_{w}) + \frac{\partial F_{en}(s,t)}{\partial s} + f_{en}(s,t) = \rho_{k}A_{k}\frac{\partial^{2}u(s,t)}{\partial t^{2}} \\ F_{en}(s,t)T_{A}(s_{w}) + \frac{\partial F_{eb}(s,t)}{\partial s} + f_{eb}(s,t) = \rho_{k}A_{k}\frac{\partial^{2}w(s,t)}{\partial t^{2}} \\ m_{\tau}(s,t)ds = \rho_{k}J_{k}\frac{\partial^{2}\varphi(s,t)}{\partial t^{2}} \end{cases}$$

$$(11)$$

$$\begin{cases} F_{A}(s,t) = F_{e\tau}(s,t) \\ M_{B}(s,t) = E_{k}I_{k} \cdot k_{C}(s,t) \\ M_{T}(s,t) = G_{k}J_{k} \cdot [\partial \varphi(s,t)/\partial s] \end{cases}$$
(12)

In a vertical well, the bending moment and torque are induced by the dynamic buckling of SRS. The critical load necessary to induce helical buckling is

$$F_{b-cr} = 2.75 \sqrt{E_s I_s (\rho_s A_s g - f_{e\tau})/r_0}$$
 (13)

When the column remains unbuckled, the additional bending moment and torque are zero. However, when buckling occurs, the maximum additional bending moment and torque (M_{Ba} and M_{Ta}) can be determined based on buckling theory (Cheng et al., 2021).

$$\begin{cases} M_{\text{Ba}} = E_{\text{s}}I_{\text{s}} \cdot 4\pi^{2}r_{0} / \left(4\pi^{2}r_{0}^{2} + p_{\text{h}}^{2}\right) \\ M_{\text{Ta}} = E_{\text{s}}J_{\text{s}}r_{0}^{2} (d\theta_{\text{b}}/dz)^{3} \end{cases}$$
(14)

$$\begin{cases} \theta_{b} = w_{0}z - w_{0}\varepsilon_{q}z^{2} / 4, p_{h} = \frac{2\pi}{d\theta_{b}/dz} = \frac{2\pi}{w_{0}(1 - \varepsilon_{q}z/2)} \\ \varepsilon_{q} = w_{0}(\rho_{s}A_{s}g - f_{e\tau}) / F_{0}, w_{0} = \sqrt{F_{0}/(2E_{s}I_{s})} \end{cases}$$
(15)

3.2. Macro-scale FEM

The objective of the macro-scale analysis is to establish the relationship between the macro load and the resultant macro stress. Although HFRP materials, similar to elastic metal materials, experience plastic deformation, the extent of this deformation is quite minimal. Prior to the fracture of the composite material, the relationship between load and strain remains almost proportional (Zhang et al., 2014; Cózar et al., 2024). Therefore, assuming a linear relationship between each component of the macro load **F** and the macro stress it induces before the failure of the HFRP rod, the macro stress within the rod can be expressed using the principle of stress superposition:

$$\overline{\sigma} = A_F F \tag{16}$$

$$\mathbf{F} = \begin{bmatrix} F_{x} & F_{y} & F_{z} & M_{x} & M_{y} & M_{z} \end{bmatrix}^{\mathrm{T}}$$

$$(17)$$

The load-stress transformation coefficient matrix A_F can be obtained from macro FEM. In practical applications, the transverse shear force F_y and F_z are substantially smaller than the longitudinal axial force F_x and can be ignore, with the rod axis considered as the X-axis. Additionally, the combined moments of M_y and M_z are treated as bending moments, with the XY plane selected as the plane of action for the bending moment. Thus, the macro load F is simplified to:

$$\mathbf{F} = [F_{X} \quad M_{X} \quad M_{Z}]^{\mathrm{T}} = [F_{\mathrm{A}} \quad M_{\mathrm{T}} \quad M_{\mathrm{B}}]^{\mathrm{T}}$$
(18)

For illustrative purposes, a HFRP rod with a diameter of 22 mm was analyzed. The macro-scale FEM of the HFRP rod was constructed with four layers, as shown in Fig. 3(a). To mitigate end effects, the model length was set as 200 mm, and results from the central section were utilized. Simulations were conducted using the WORKBENCH. Material parameters for the cylindrical composite were assigned within the cylindrical CS (local CS), as depicted in Fig. 3(b). The stiffness matrix $\overline{\bf Q}$ for each material layer was computed using Eq. (6) and Eq. (7), based on the material engineering elastic coefficients listed in Table 3. The mesh was generated using the sweep method, with a refined mesh applied to the GFRP winding layer, as illustrated in Fig. 3(a). Adjacent layers were bound to ensure contact, and a fixed constraint was applied to the bottom of the model. A load was applied to the upper end of the model, as shown in Fig. 3(c). By applying the unit components of

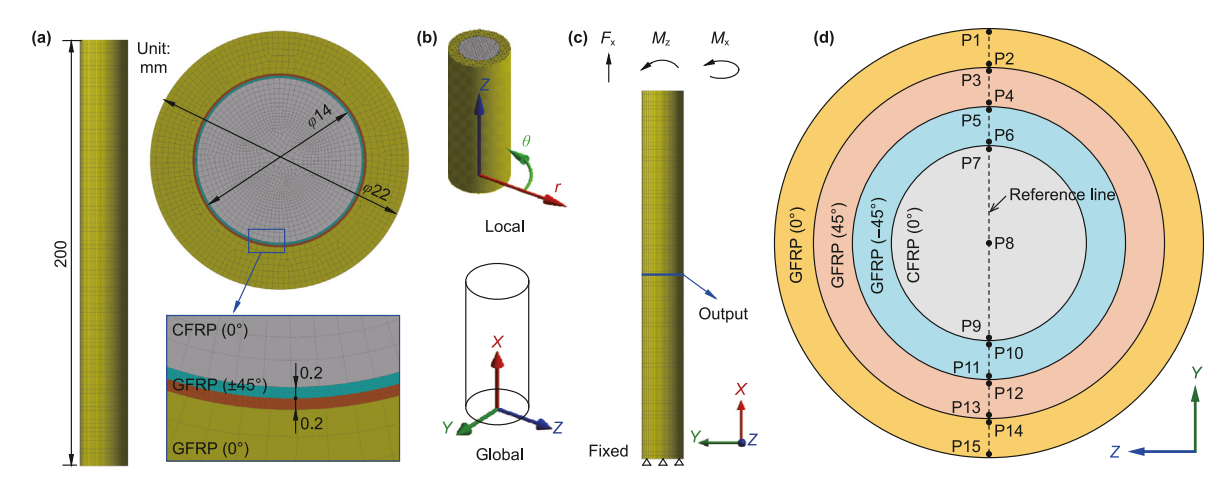


Fig. 3. Macro-scale FEM and macro critical points of HFRP rod. (a) Gemetric model and meshing; (b) Coordinate systems; (c) Constraints and loading; (d) Macro critical points.

load F, the load-stress transformation coefficient matrix for each point within the HFRP rod was determined. Mesh independence analysis confirmed that the macro FEM required approximately 7.0×10^5 elements.

Given the axial symmetry of the HFRP rod, the stress components induced by tensile and torsional loads are solely functions of the polar radius r. Furthermore, the main stress component due to bending load will attain an peak value within its plane of action (XY plane). Consequently, the intersection of the action plane of bending moment and the mid-cross section of the model is designated as the reference line, as illustrated in Fig. 3(d). Fifteen macro critical points are identified along this reference line for assessing the failure of the HFRP rod.

3.3. Meso-scale FEM

The meso stress of fiber and matrix is necessary to assess the failure of an HFRP rod using the MMF method. Due to the differing mechanical properties of the fiber and matrix, the meso stresses resulting from macro stresses may become highly concentrated in specific regions. Consequently, a stress amplification factor is introduced to characterize the relationship between macro stresses and meso stresses.

$$\begin{cases}
\widehat{\boldsymbol{\sigma}} = \boldsymbol{A}_{\boldsymbol{\sigma}} \overline{\boldsymbol{\sigma}} \\
\overline{\boldsymbol{\sigma}} = [\overline{\sigma}_{1} \quad \overline{\sigma}_{2} \quad \overline{\sigma}_{3} \quad \overline{\tau}_{23} \quad \overline{\tau}_{31} \quad \overline{\tau}_{12}]^{\mathrm{T}} \\
\widehat{\boldsymbol{\sigma}} = [\widehat{\sigma}_{1} \quad \widehat{\sigma}_{2} \quad \widehat{\sigma}_{3} \quad \widehat{\tau}_{23} \quad \widehat{\tau}_{31} \quad \widehat{\tau}_{12}]^{\mathrm{T}}
\end{cases} \tag{19}$$

The stress amplification factor \mathbf{A}_{σ} can be determined using a RVE, which is a meso FEM composed of multiple repeated unit cells (RUCs) that characterize the distribution of fibers within the matrix. To ascertain this distribution, a cross-section of the HFRP rod is analyzed using a SEM, as depicted in Fig. 4(a). The analysis reveals that the fibers are not uniformly distributed throughout the matrix. For modeling purposes, it was assumed that the fibers were uniformly distributed and securely bonded to the matrix. Consequently, RUCs with two typical distribution patterns—square and hexagonal—are established for meso stress analysis, as shown in Fig. 4(b) and (c). Based on the fiber-to-matrix ratio, the fiber diameter is set at 200 mm, while the side lengths of the regular quadrilateral and hexagon are 211.8 mm and 131.4 mm, respectively. Failure evaluation is conducted based on the maximum stress experienced by the fiber and matrix in these two distribution configurations. The dimensions of the RUCs are determined by the

volume ratio of fiber to resin. For the square and hexagonal RUCs, 16 and 20 meso critical points are selected, respectively, to assess the failure of the fiber and matrix.

Two meso-scale FEM, as illustrated in Fig. 5(a), are developed based on the square and hexagonal RUCs. To mitigate errors due to loading end effects, multiple RUCs are utilized to construct the square and hexagonal RVEs for CFRP and GFRP. The geometric models of the RVEs are cubic, with side lengths of 653.4 mm and 682.7 mm, respectively. The specific dimensions are detailed in Fig. 5(a). Hexagonal mesh and scanning methods are used for meshing. And mesh independence analysis determines that the optimal number of elements for the square RVE and hexagonal RVE are 6.4×10^5 and 6.9×10^5 , respectively. Results from the middle RUC in the middle section of meso FEM are used for analysis, as shown in Fig. 5(c). Material parameters for the fiber and resin in the meso-scale FEM are assigned according to the data presented in Table 2. The overlapping interfaces of the fibers and resin are set for bonding. And the macro stress applied to the meso-scale FEM comprises six stress components, with the application method (Li et al., 2013) for each stress component illustrated in Fig. 5(b).

When calculating the meso stress of the fiber and matrix, it is essential to convert the macro stress components from the cylindrical CS to the rectangular CS. The stress transformation relationship is given by:

$$\begin{cases} \overline{\sigma}_{R} = T_{CR}\overline{\sigma}_{C} \\ \overline{\sigma}_{R} = \begin{bmatrix} \sigma_{x} & \sigma_{y} & \sigma_{z} & \tau_{yz} & \tau_{zx} & \tau_{xy} \end{bmatrix}^{T} \\ \overline{\sigma}_{C} = \begin{bmatrix} \sigma_{r} & \sigma_{\theta} & \sigma_{z} & \tau_{\theta z} & \tau_{zr} & \tau_{r\theta} \end{bmatrix}^{T} \end{cases}$$
(20)

The global rectangular CS (x-y-z) for the macro-scale FEM and the macro stress CS (1-2-3) for the CFRP core and GFRP coating are aligned, so the macro stress applied to the RVE is same as that in the global rectangular CS. However, the above two CSs are different in the GFRP winding layer. Consequently, the macro stress applied to the RVE of the GFRP winding must be transformed.

The macro stress CS (1-2-3) for the GFRP winding layer can be viewed as a global CS (x-y-z) rotated by a certain angle β around the Y-axis. Thus, the stress transformation formula is expressed as:

$$\overline{\sigma} = T_{\nu\beta}\overline{\sigma}_{R} \tag{21}$$

As shown in Fig. 4(a), the CS 1'-2'-3' of each RVE differs from the macro stress CS 1-2-3. Therefore, macro stresses applied to the meso-scale FEM must be transformed accordingly. The CS 1'-2'-3'

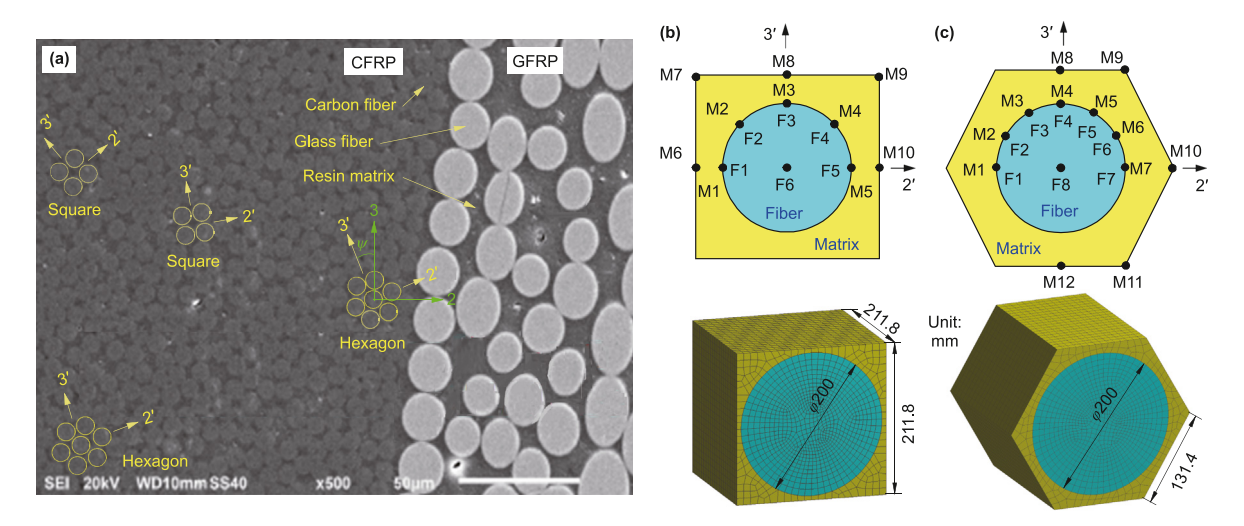


Fig. 4. Schematic diagram of RUC and meso critical points. (a) SEM pictures of HFRP cross section; (b) Square RUC; (c) Hexagon RUC.

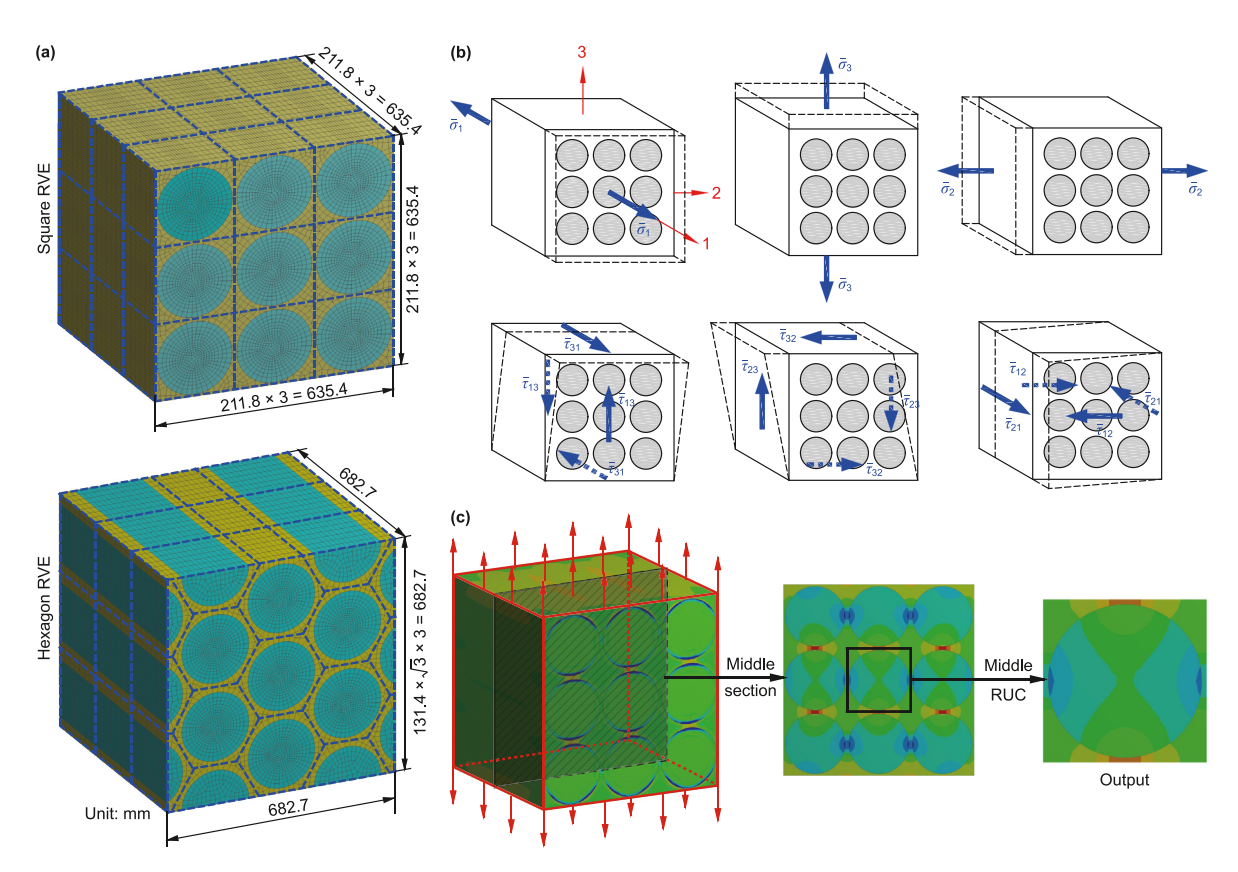


Fig. 5. Meso-scale FEM of fiber and matrix. (a) Meso-scale FEM of RVEs; (b) Macro stress component application in meso-scale FEM; (c) Output results of meso-scale FEM.

can be obtained by rotating the CS 1-2-3 around axis 1 by a certain angle (ψ) , thus the transformation formula is:

 $\widehat{\boldsymbol{\sigma}} = \boldsymbol{A}_{\sigma} \boldsymbol{T}_{1\psi} \overline{\boldsymbol{\sigma}} \tag{22}$

3.4. Dual-scale failure criterion of HFRP rod

Following the above analytical framework, the meso stress for

each meso critical point of each macro critical point within each layer of the HFRP rod can be obtained.

$$\hat{\boldsymbol{\sigma}} = \boldsymbol{A}_{\sigma} \boldsymbol{T}_{1\psi} \boldsymbol{T}_{y\beta} \boldsymbol{T}_{CR} \boldsymbol{A}_{F} \boldsymbol{F} \tag{23}$$

Based on Eq. (23), the meso stresses of both the fiber and matrix under complex macro loads can be directly computed, facilitating subsequent failure evaluation using MMF method. The strength margin of HRPS rod serves as the basis for this failure assessment. The detailed procedure is as follows:

First, the strength margin for each meso critical point within the

RUC is computed individually using Eq. (24) and Eq. (25):

$$\eta_{Fi} = \begin{cases}
1 - \widehat{\sigma}_{f1} / \sigma_{ft} & \sigma_{f1} > 0 \\
 & i = 1, 2, \dots, 6 \text{ or } 8 \\
1 - \widehat{\sigma}_{f1} / \sigma_{fc} & \sigma_{f1} \le 0
\end{cases}$$
(24)

$$\eta_{\rm Mj} = 1 - \left[(J_1/J_{1-{\rm cr}}) + (\sigma_{\rm VM}/\sigma_{\rm VM-{\rm cr}})^2 \right] \quad j=1,\cdots,10 \ {
m or} \ 12$$
 (25)

Then, the minimum strength margin among all meso critical points within the RUC is used to represent the strength margin of the corresponding macro critical point of the HFRP section:

$$\eta_{\mathsf{L}k} = \min\{[\eta_{\mathsf{F}i}] \cup [\eta_{\mathsf{M}i}]\} \quad k = 1, 2, \dots, 15$$

Finally, the minimum strength margin across all macro critical points is taken as the overall strength margin of the HFRP rod. If the strength margin of the HFRP rod is less than zero, the HFRP rod is deemed to have failed:

$$\eta_{\mathsf{A}} = \min\{[\eta_{\mathsf{L}k}]\}\tag{27}$$

By following this analysis process, the relationship between the strength margin of the HFRP rod and its macro load can be established, represented by:

$$\eta_{A} = f_{A}(F_{A}, M_{T}, M_{B}) \tag{28}$$

3.5. Equivalent fatigue failure evaluation method for HFRP rod joint

3.5.1. Potential failure points in HFRP rod joints

As depicted in Fig. 1, the HFRP rod joint primarily comprises a coupling, a rotary joint, and an adhesive joint. One end of the joint is attached to a weighted steel rod or a polished rod via the coupling, while the other end connects to the HFRP rod through an adhesive joint secured with resin adhesive.

Given the prevalence of various failure modes in HFRP rod joints in practical applications, a comprehensive analysis of potential failure points is essential. A three-dimensional comprehensive FEM of the joint has been developed, as illustrated in Fig. 6. This model includes mesh division and material parameters for the HFRP rod, consistent with those outlined in Section 3.3. The elastic modulus for the steel joints, including the coupling, rotary joint, and adhesive joint, is set at 210 GPa, while the resin adhesive has an elastic modulus of 4 GPa. The Poisson's ratios for these materials are 0.3 and 0.38, respectively. Each contact surface is modeled as a bonded interface, with the coupling end fixed and the HFRP rod subjected to individual tensile, torsional, and bending loads. Utilizing this comprehensive FEM, stress distribution patterns for the HFRP rod, steel joint, and resin adhesive under unit tensile and bending moment loads have been analyzed and are presented in Fig. 7.

Fig. 7(a) shows the distribution of axial normal stress σ_z in the

HFRP rod at the joint and shear stress $\tau_{\theta z}$ under unit torque. The figure reveals a significant stress concentration in the H1 cross-section of the HFRP rod near the adhesive joint outlet. The principal stress distributions in the cross-section H1 are depicted in Fig. 7(d). The maximum stress is observed at the outer edge of the GFRP coating, making this region prone to potential failure. Therefore, the H1 cross-section is identified as a critical area for assessing joint failure. The potential failure points on the H1 cross-section are included in macro critical points, allowing the dual-scale method constructed in Section 2 to be used to analyze the failure of the HFRP rod at the joint.

Fig. 7(b) illustrates a notable concentration of stress at the necking of the rotary joint. For instance, at point S1, the von Mises stress under unit tensile, torsional, and bending loads are projected to be 2002 kPa, 642 kPa, and 750 kPa, respectively. Under real operational conditions, these stress levels are susceptible to approaching the material's strength limit, thereby increasing the likelihood of failure. Consequently, points S1–S4 have been identified as potential failure points for the joint.

The von Mises stress distribution of the resin adhesive within the groove is depicted in Fig. 7(c). The results show a pronounced stress concentration at the sharp corners of the adhesive, particularly in the first adhesive groove on the left side. The von Mises stresses of the resin adhesive bonded to the HFRP rod are detailed in Fig. 7(e). It is evident that the resin adhesive in the first two grooves on the left endures the majority of the applied loads. Simulation results indicate that the resin adhesive in these two grooves sustains 55.4% of the tensile load, 57.0% of the torsional load, and 78.2% of the bending load, respectively. The stress concentration at the sharp corners increases the likelihood of the resin adhesive detaching from the HFRP rod at points A1 or A2, leading to joint failure. Therefore, points A1 and A2 are identified as critical locations for assessing joint failure.

3.5.2. Equivalent fatigue strength of HFRP rod joints

Based on the relationship between fatigue life and fatigue stress for a $\phi 22$ mm HFRP rod, as determined experimentally by Li et al. (2019a), the axial fatigue strength of the HFRP rod can be derived. This is calculated as the maximum average axial stress corresponding to a specified number of fatigue cycles.

$$\sigma_{-1} = \sigma_{\text{UTS}} \cdot 10 \left(\frac{3.992 - \lg N_{f0}}{3.919} \right) \tag{29}$$

Upon application of bending moments and torques to a HFRP rod, both its tensile strength and fatigue strength are reduced. Assuming a consistent pattern of reduction, the equivalent fatigue strength of the HFRP rod can be expressed as

$$\sigma_{-1E} = f_{TB}(m_T, m_B) \cdot \sigma_{-1} \tag{30}$$

where, $f_{\text{TB}}(\cdot)$ is the influence function of bending moment and torque on the tensile capacity of HFRP rod, which can be obtained by the dual scale failure evaluation method.

Therefore, the fatigue strength margin (FSM) of the HFRP rod

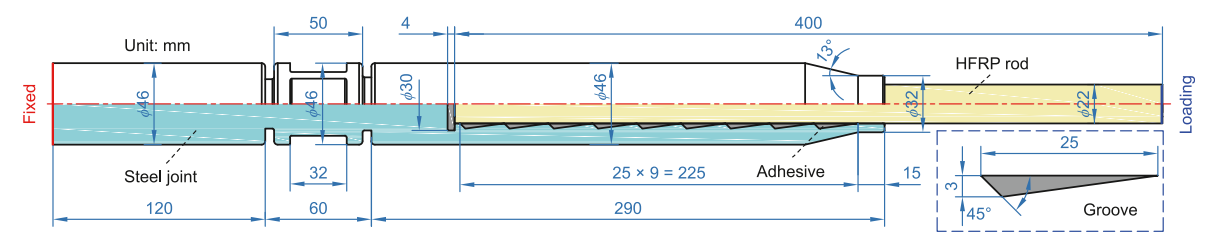


Fig. 6. Macro FEM of HFRP rod joints.

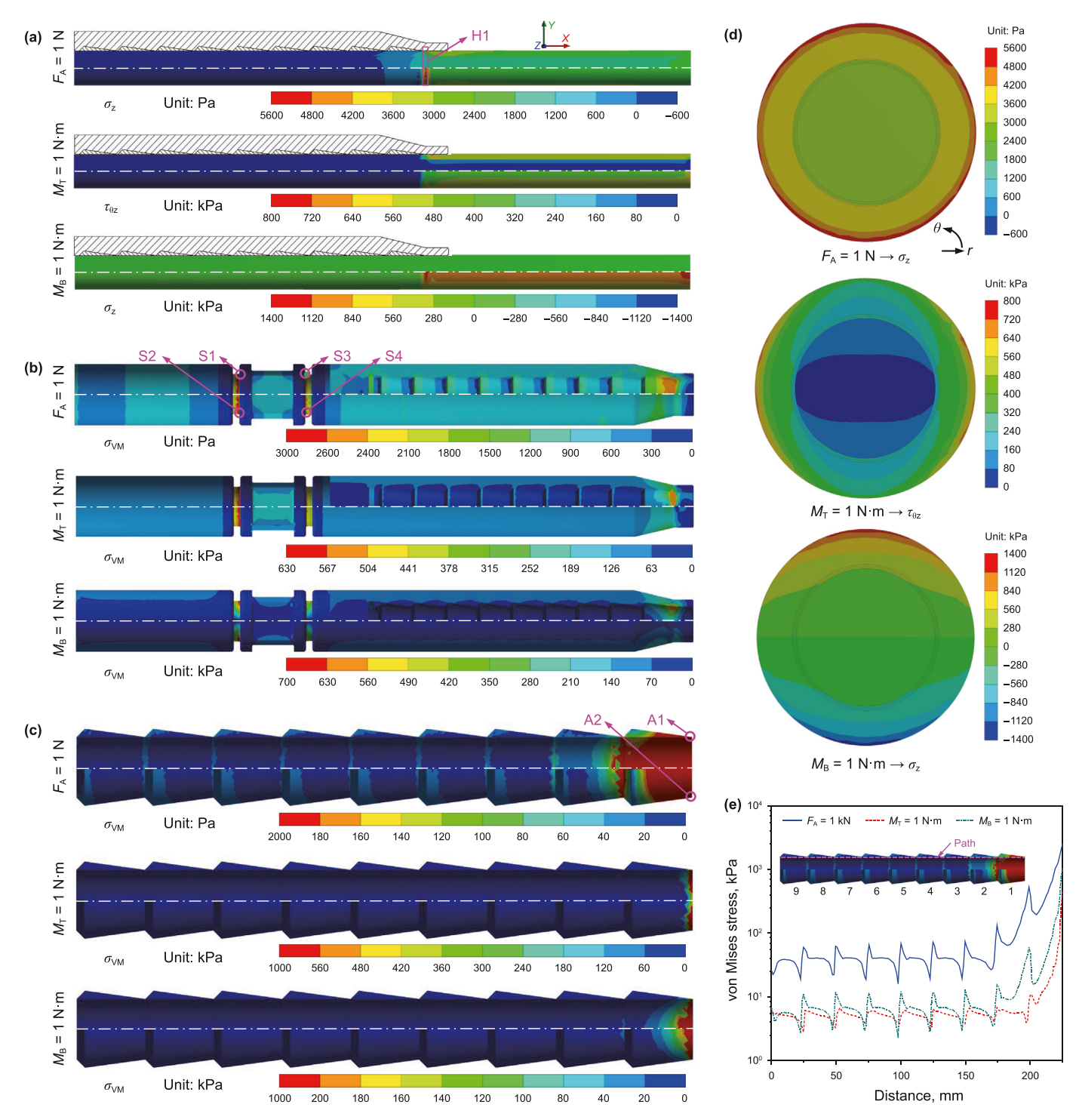


Fig. 7. Macro stress distribution at the HFRP joint. (a) HFRP rod at joints; (b) steel joints; (c) Adhesive; (d) Section H1; (e) Adhesive bonded to HFRP rods.

subjected to complex loading conditions can be determined as follows:

$$\begin{cases} \zeta_{HR} = 1 - \frac{F_{A}/A_{H}}{\sigma_{-1E}} = 1 - \frac{F_{A}/A_{H}}{\sigma_{-1} \cdot f_{TB}^{R}(M_{T}/M_{T-cr}, M_{B}/M_{B-cr})} \\ \zeta_{HJ} = 1 - \frac{F_{A}/A_{H}}{\sigma_{-1E}} = 1 - \frac{F_{A}/A_{H}}{\sigma_{-1} \cdot f_{TB}^{J}(M_{T}/M_{T-cr}, M_{B}/M_{B-cr})} \end{cases}$$
(31)

The steel joints and resin adhesives present potential failure

points that must be considered when evaluating the fatigue failure of the joints. Based on the simulation results from the comprehensive FEM of the HFRP rod joint, the relationship between macro loads and the stress at potential failure points within the steel joint and resin adhesive is derived.

$$\begin{cases}
\sigma_{Si} = \mathbf{A}_{Si}\mathbf{F} & i = 1, 2, 3, 4 \\
\sigma_{Aj} = \mathbf{A}_{Aj}\mathbf{F} & j = 1, 2
\end{cases}$$
(32)

The FSM of the steel joints and resin adhesives under complex loading conditions can be determined based on the stress vectors at these potential failure points.

$$\begin{cases} \zeta_{S} = \min\{1 - PL_{Si}\} & i = 1, 2, 3, 4 \\ \zeta_{A} = \min\left\{1 - \sigma_{VM-Aj} / [\sigma_{A}]\right\} & j = 1, 2 \end{cases}$$
(33)

$$PL_{Si} = \left(\sigma_{VM-Si}^{max} - \sigma_{VM-Si}^{min}\right) / \left([\sigma_{S}] - \sigma_{VM-Si}^{min}\right)$$
(34)

$$[\sigma_{\rm S}] = \delta_{\rm A} \left(0.25 \sigma_{\rm Sb} + 0.5625 \sigma_{{\rm VM-S}i}^{\rm min} \right)$$
 (35)

The FSM of the joint, denoted as ζ_J , is determined by the minimum FSM among the steel joint, resin adhesive, and the HFRP rod at the joint. If ζ_I is less than zero, the joint is deemed to have failed.

$$\zeta_{I} = \min\{\zeta_{HI}, \zeta_{A}, \zeta_{S}\}$$
(36)

4. Result analysis of dual-scale failure evaluation method

4.1. Macro stress analysis

The macro stress components at each point along the reference line cause by a single macro load component are illustrated in Fig. 8.

The order of magnitude for stress generated by axial tensile force $(F_{\rm A})$ of 1000 N is equivalent to that of bending moment and torque $(M_{\rm B}$ and $M_{\rm T})$ of 1 N m. FA and MB primarily generate axial and tangential normal stress $(\overline{\sigma}_{\rm Z}$ and $\overline{\sigma}_{\theta})$. Furthermore, the maximum values of $\overline{\sigma}_{\rm Z}$ and $\overline{\tau}_{\rm TZ}$ resulting from $F_{\rm A}$ and $M_{\rm B}$ are observed in the CFRP core layer, while the peak values of other macro stress components are found at the inner or outer interfaces of the GFRP winding layer. $M_{\rm T}$ predominantly induces macro shear stress $\overline{\tau}_{\theta Z}$, with its peak values occurring at the outer edges of the GFRP winding layer and at the inner and outer interfaces of the GFRP coating layer. The locations where these maximum macro stress components are included in the selected macro critical point set, indicating that the failure of the HRPS rod can be effectively assessed based on the stress states at these macro critical points.

4.2. Meso stress analysis

Using CFRP material as an illustrative example, Fig. 9(a) depicts the distribution of meso stress components induced by unit macro normal stress $\overline{\sigma}_1$ within a square RUC, while Fig. 9(b) presents the distribution of meso normal stress $\widehat{\sigma}_1$ resulting from each unit macro stress component. As illustrated in Fig. 9(a), the macro normal stress $\overline{\sigma}_1$ predominantly induces meso normal stress $\widehat{\sigma}_1$, which mainly borne by the fiber. The other meso stress components induced by $\overline{\sigma}_1$ are relatively minor and exhibit similar magnitudes in both the matrix and fiber. Specifically, the maximum value of meso normal stress $\widehat{\sigma}_1$ is observed at the fiber edge in the 45° and

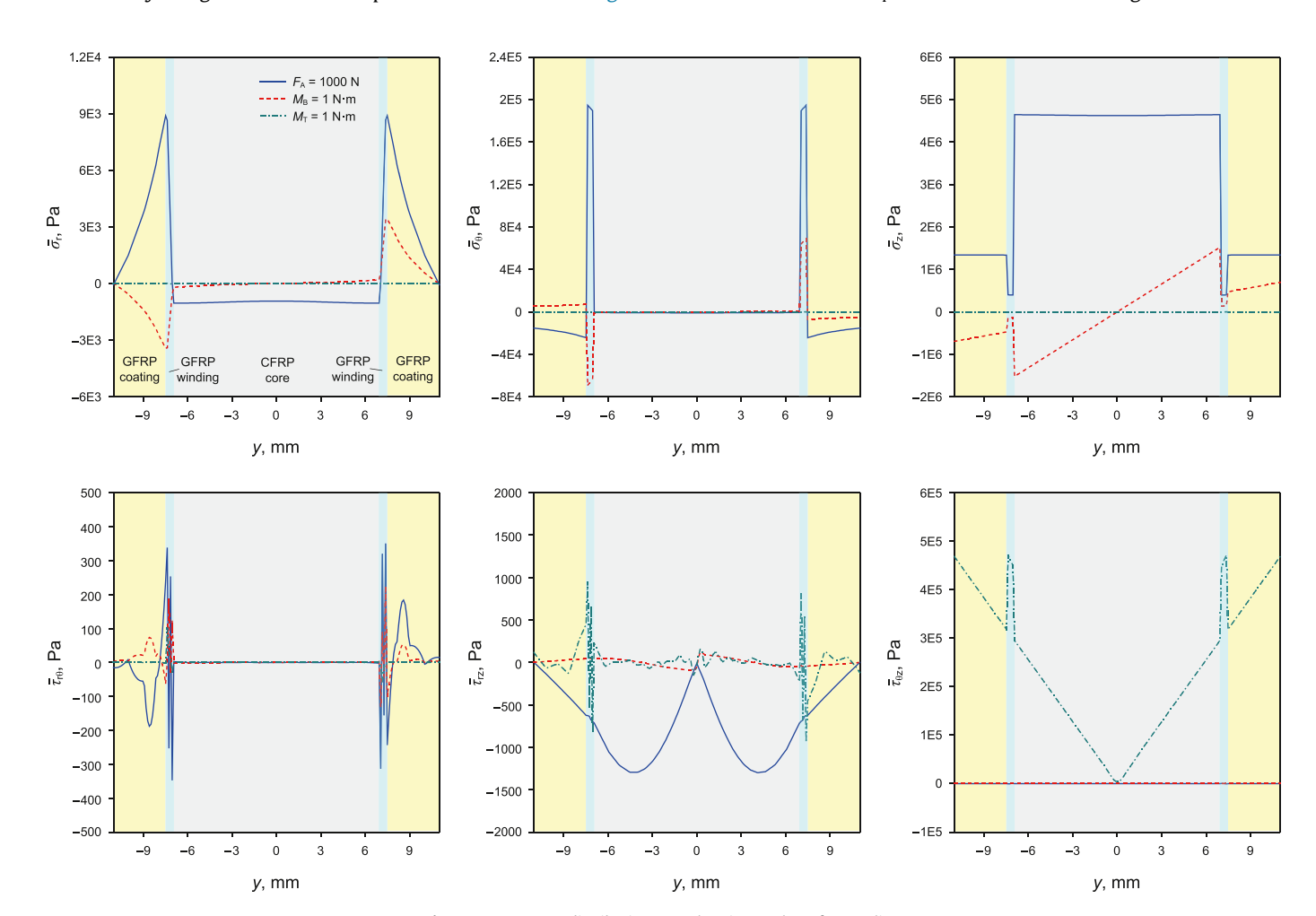


Fig. 8. Macro stress distribution at each point on the reference line.

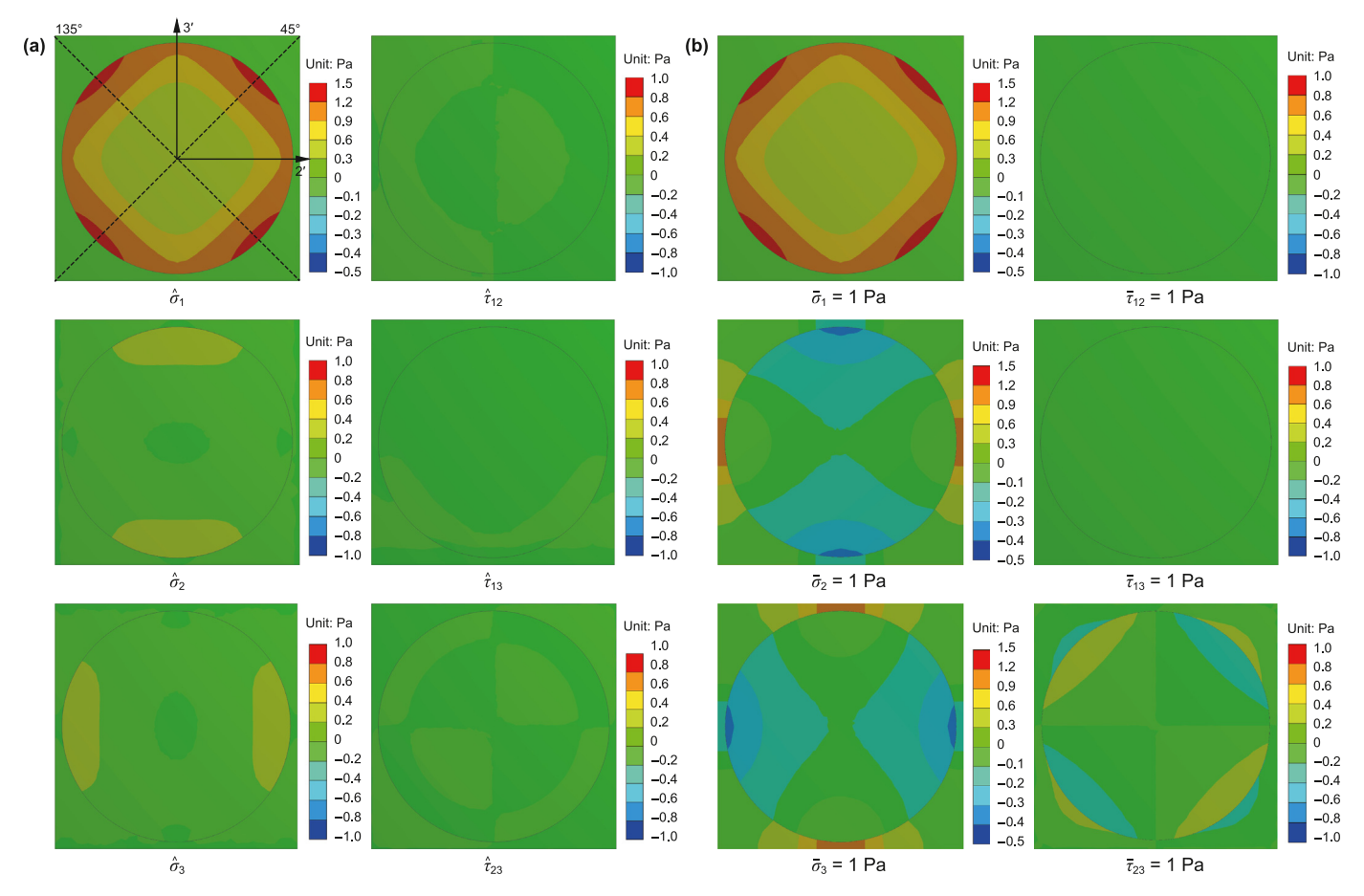


Fig. 9. Distribution of meso stress components in square RUC. (a) Meso stress components caused by unit macro stress $\overline{\sigma}_1$; (b) Meso normal stress $\hat{\sigma}_1$ caused by each unit macro stress.

135° directions, whereas the maximum values for $\widehat{\sigma}_2$ and $\widehat{\sigma}_3$ are found at 90° and 0°, respectively. Fig. 9(b) shows that the meso stress $\widehat{\sigma}_1$ resulting from the unit macro stress $\overline{\sigma}_2$ is positive in the 0° direction and negative in the 90° direction. Conversely, the meso stress $\widehat{\sigma}_1$ resulting from the unit macro stress $\overline{\sigma}_3$ exhibits an opposite pattern. The unit macro shear stresses $\overline{\tau}_{12}$ and $\overline{\tau}_{13}$ generally do not generate significant meso stress $\widehat{\sigma}_1$, whereas the unit macro shear stress $\overline{\tau}_{23}$ induces a higher meso stress $\widehat{\sigma}_1$, reaching peak values in the 45° and 135° directions. The locations of maximum meso stress are incorporated into the selected meso critical points.

In the case of the hexagonal RUC of CFRP, Fig. 10 illustrates the distribution of meso stress components. As depicted in Fig. 10(a), the meso stress $\hat{\sigma}_1$ resulting from the unit macro stress $\overline{\sigma}_1$ is the predominant component within the hexagonal RUC, primarily borne by the fiber. Notably, the maximum value of this stress occurs in the 90° direction. Other meso stress components induced by unit macro stress $\overline{\sigma}_1$ are relatively small, consistent with the findings observed in the square RUC. Fig. 10(b) reveals that the meso normal stress $\hat{\sigma}_1$ caused by unit macro stress $\overline{\sigma}_2$, $\overline{\sigma}_3$, $\overline{\tau}_{12}$, $\overline{\tau}_{13}$ and $\overline{\tau}_{23}$ aligns closely with the results obtained for the square RUC. However, the peak meso stresses in both the fiber and matrix are observed in the directions of 0° , 30° , 60° , 90° , 120° , 150° and 180° . The locations of maximum meso stress within the hexagonal RUC are also included in the selected meso critical points. This suggests that the stress states at these selected meso critical points can effectively evaluate the failure mechanisms in CFRP and GFRP composites.

Based on the meso-scale stress analysis, stress amplification factors for meso critical points in square and hexagonal RUC of CFRP and GFRP composites can be obtained. The stress amplification factor matrices of F2 and M2 points in the square RUC of CFRP composites are given by:

$$\boldsymbol{A}_{\sigma}^{\text{SCF2}} = \begin{bmatrix} 1.39 & -0.10 & -0.18 & 0.22 & 0 & 0 \\ -0.02 & 1.02 & 0.03 & 0.42 & 0 & 0 \\ -0.02 & 0.19 & 0.80 & 0.47 & 0 & 0 \\ 0 & 0.08 & 0.01 & 1.26 & 0 & 0 \\ 0 & 0 & 0 & 0 & 0.95 & 0.60 \\ 0 & 0 & 0 & 0 & 0.35 & 1.26 \end{bmatrix},$$

$$\boldsymbol{A}_{\sigma}^{\text{SCM2}} = \begin{bmatrix} 0.00 & 0.09 & 0.03 & -0.04 & 0 & 0 \\ -0.01 & 0.20 & -0.01 & 0 & 0 & 0 \\ 0 & 0.05 & 0.11 & -0.11 & 0 & 0 \\ 0 & 0.02 & -0.03 & 0.13 & 0 & 0 \\ 0 & 0 & 0 & 0 & 0.03 & -0.07 \\ 0 & 0 & 0 & 0 & -0.03 & 0.14 \end{bmatrix}$$
 (37)

According to Eq. (37), $\mathbf{A}_{\sigma}^{\text{SCF2}}$ is a diagonally dominant matrix, which indicates that each macro stress component at the F2 point on the fiber predominantly results in the corresponding meso stress component. The diagonal elements of $\mathbf{A}_{\sigma}^{\text{SCF2}}$ suggest that when macro stresses $\overline{\sigma}_1$, $\overline{\sigma}_2$, $\overline{\tau}_{12}$ and $\overline{\tau}_{23}$ are applied at the F2 point, they are amplified when transformed into corresponding

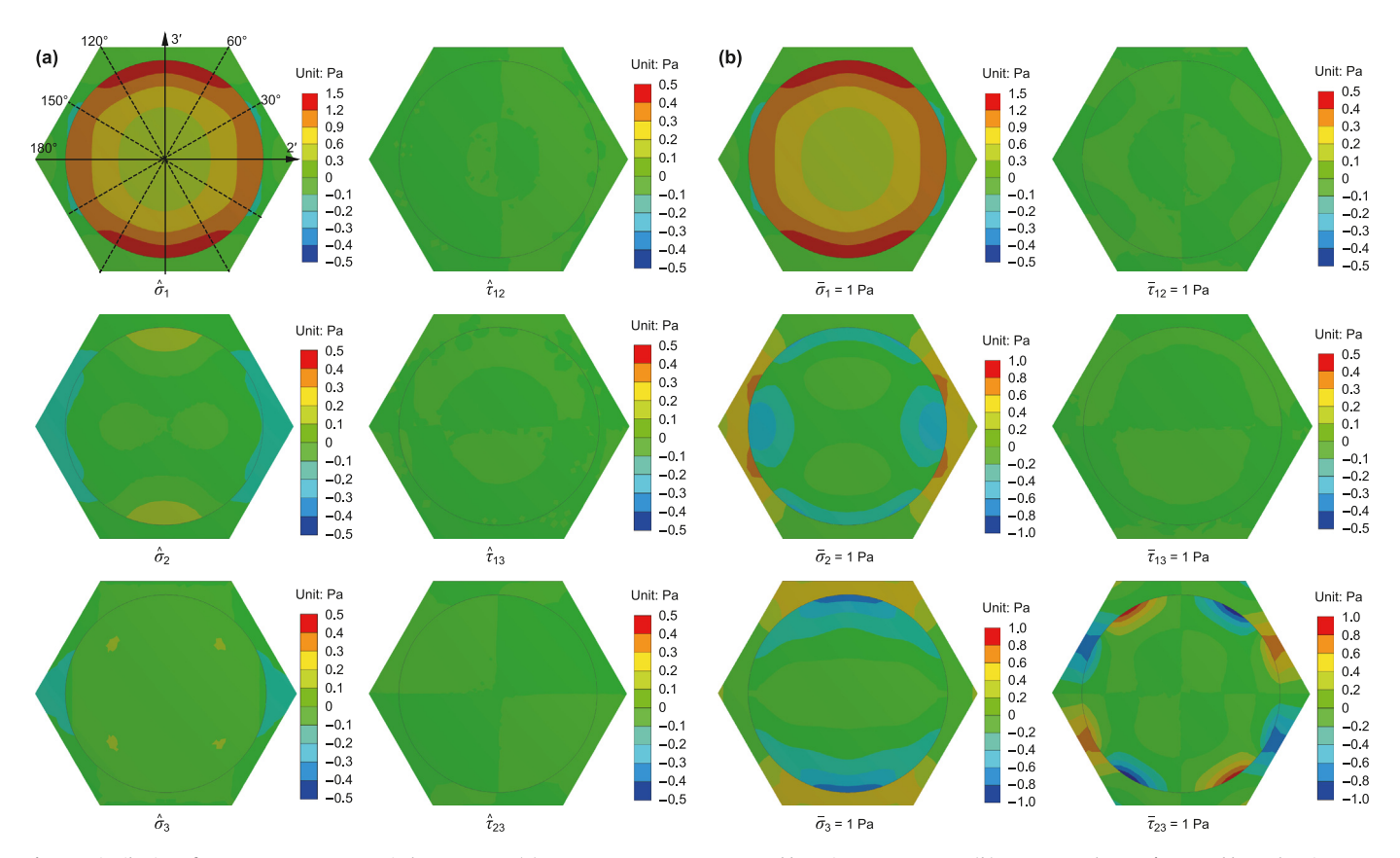


Fig. 10. Distribution of meso stress components in hexagon RUC. (a) Meso stress components caused by unit macro stress $\overline{\sigma}_1$; (b) Meso normal stress $\hat{\sigma}_1$ caused by each unit macro stress.

meso stresses, whereas other macro stress components are reduced. The absolute values of the elements in A_{σ}^{SCM2} are less than 0.2, implying that at the M2 point in the resin matrix, all macro stress components are significantly reduced upon transformation into meso stresses.

The impact of the rotation angle ψ on the meso stress components induced by macro normal stress $\overline{\sigma}_1$ at the F1 point in both square and hexagonal RVEs is illustrated in Fig. 11. In both RVEs, the rotation angle ψ significantly affects the meso stress components $\widehat{\sigma}_2$, $\widehat{\sigma}_3$ and $\widehat{\tau}_{12}$, which may influence the values of σ_{F1} , J_1 and σ_{VM} for fiber and matrix failure assessment. Consequently, it is imperative to analyze the meso stresses for both matrix and fiber across a range of rotation angles ψ , from 0° to 180° , and to perform failure

evaluations based on the most severe meso stress conditions.

By utilizing the meso FEM along with Eqs. (24) and (25), the strength margins for critical micro points in unidirectional CFRP and GFRP under an fiber axial macro stress $\overline{\sigma}_{10}$ (1-axis direction in Fig. 2(b)) of 1000 MPa were obtained, as shown in Fig. 12. The strength margin of the matrix in CFRP is relatively close to that of the fibers, with the minimum margin occurring at point M1. In contrast, the matrix strength margin in GFRP is significantly lower than that of the fibers, also with the minimum margin at point M1. Specifically, the minimum strength margins for CFRP and GFRP are 0.562 and 0.165, respectively. Based on definitions, $\sigma_b = \overline{\sigma}_{10}(1 - \eta_{\text{CFRP}}^{\text{min}})$. Thus, the FATS of CFRP and GFRP are calculated to be 2283.1 MPa and 1197.6 MPa, respectively.

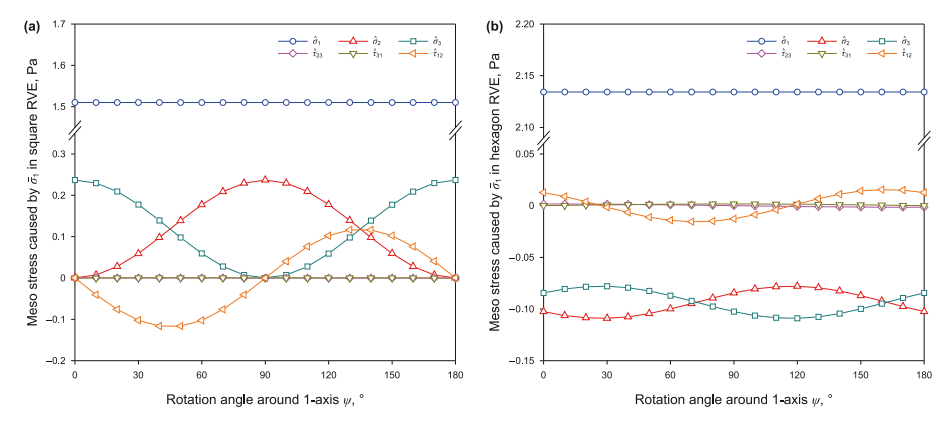


Fig. 11. Effect of angle ψ on meso stress component in RVE. (a) F1 point in square RVE of CFRP; (b) F1 point in hexagon RVE of CFRP.

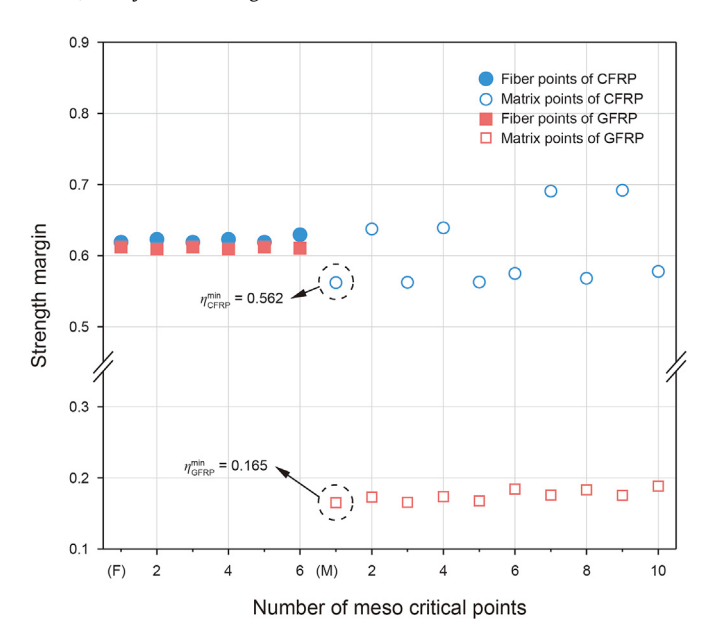


Fig. 12. Strength margin of meso critical points.

4.3. Prediction of the critical load for HFRP rod

Using the dual-scale failure evaluation method established in Section 2, the effect of individual loads on the strength margin η_A of the φ 22 mm HFRP rod was calculated according to Eqs. (23)–(28), the results are illustrated in Fig. 13(a). The critical tensile load (F_{A-CT}) for φ 22 mm HFRP rod is 340.2 kN, the critical bending load (M_{B-CT}) is 1192.4 N m, and the critical torsional load (M_{T-CT}) is 132.3 N m. The results suggest that the HFRP rods are most sensitive to torsional loads, as the resin matrix experiences stress comparable to that of the fibers during torsion, while the stresses generated by tensile and bending loads are predominantly borne by the fibers.

Fig. 13(b) presents the strength margin at various macro critical points on a φ 22 mm HFRP rod under critical loads. The strength margin of the GFRP winding layer drops to zero initially due to critical tensile and bending loads, as these primarily induce axial tensile or compressive stresses along the rod's axis. In the CFRP core layer and the GFRP coating layer, these axial stresses align with the fibers, where the fibers effectively bear the majority of the load. Conversely, the GFRP winding layer experiences off-axis tensile or compressive stresses, more likely to reach the resin matrix failure threshold. Consequently, the winding layer is particularly

susceptible to failure under tensile and bending loads. Under torsional loads, shear stress peaks at the outer edge of the GFRP coating layer, where the resin matrix endures stress similar to the fibers, making the coating layer the most prone to failure under twisting.

4.4. Effect of bending moment and torque on tensile capacity for HFRP rods at joints

HFRP rods may be subjected to bending moments and torques during operation (Wang and Dong, 2021; Wang et al., 2024), which can reduce their axial tensile capacity. Therefore, it is essential to evaluate the effects of bending moments and torques on both the tensile capacity of the HFRP rods and HFRP rods at joints. Using Eqs. (23)—(28), the critical tensile load of HFRP rods and HFRP rods at joints under varying bending moments and torques can be determined, as shown in Fig. 14.

Fig. 14(a) illustrates that the critical tensile load (F_{AC-cr}) of the HFRP rod decreases gradually with increasing torque, with a significant decline occurring only as the torque approaches its critical value. This behavior is attributable to the differing critical points for torsional and tensile loads. Conversely, the critical points under bending loads coincide with those under tensile loads, resulting in a rapid, linear decrease in the critical tensile load as the bending moment increases. Fig. 14(b) further reveals that the effects of bending moments and torques on the axial tensile capacity (F_{AJC-cr}) of the HFRP rods at the joints are similar to those on the rod body. However, due to stress concentration at the joint, the critical tensile load (F_{AI-cr}) is reduced to 61% of the rod body, the critical bending moment $(M_{\rm BI-cr})$ is reduced to 12%, and the critical torque $(M_{\rm TI-cr})$ is reduced to 82%. These findings indicate that the stress concentration at the joint significantly diminishes the tensile, torsional, and bending capacities of the HFRP rod, with the most pronounced reduction observed in bending ability.

To quantitatively assess these effects, Eq. (38) was employed to model the degree of impact of bending moments and torques on the tensile capacity of HFRP rods and the HFRP rods at the joints. The resulting fitting coefficients are presented in Table 4, where fR TB and fJ TB represent the effect function of HFRP rods and HFRP rods at joints, respectively.

$$\begin{cases} f_{TB}(m_T, m_B) = c_0 + c_1 m_T + c_2 m_B + c_3 m_T^2 + c_4 m_T m_B + \\ c_5 m_B^2 + c_6 m_T^3 + c_7 m_T^2 m_B + c_8 m_T m_B^2 + c_9 m_B^3 \\ m_T = M_T / M_{T-cr}, m_B = M_B / M_{B-cr} \end{cases}$$
(38)

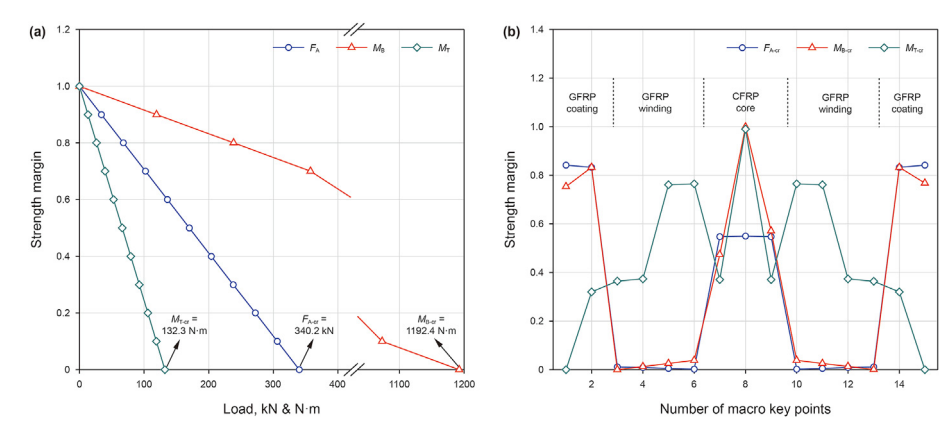


Fig. 13. Effect of individual load on the strength margin of HFRP. (a) Prediction of static critical load; (b) Strength margin of macro critical. points under critical load.

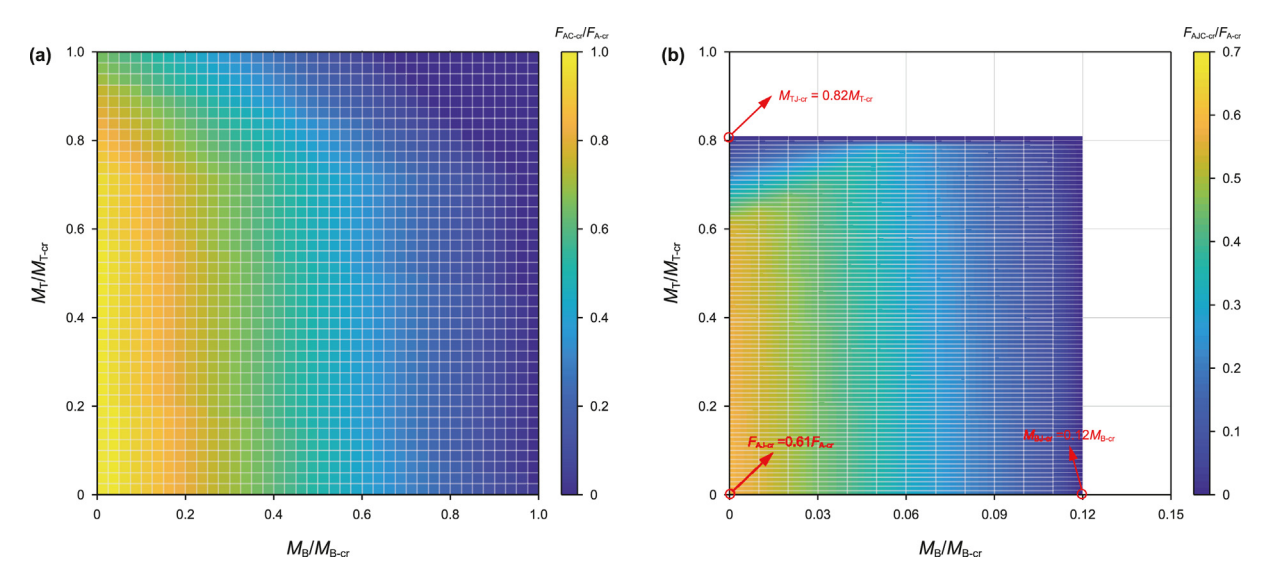


Fig. 14. Effect of bending moment and torque on tensile capacity. (a) HFRP rods; (b) HFRP rods at joints.

Table 4 Fitting coefficient of function $f_{\rm TB}$ for HFRP rod and HFRP rod at joint.

Coefficients	c_0	c ₁	c_2	<i>c</i> ₃	<i>c</i> ₄	c ₅	c ₆	c ₇	c ₈	<i>c</i> ₉
HFRP rod, fR TB	0.95	-0.03	-0.60	1.02	-1.29	-0.64	-1.47	1.06	0.54	0.34
HFRP rod at joint, fJ TB	0.58	0.02	-3.49	0.78	-3.23	20.18	-1.90	13.86	-35.49	132.20

4.5. Prediction of critical fatigue load for joints

Using a HFRP rod with a diameter of 22 mm and its joint as a case study (with the steel joint material matching that of D-grade steel sucker rods, which have a tensile strength of 880 MPa; and the resin adhesive with a fatigue strength of 105 MPa, $N_{\rm f0}=10^6$), the FSM of HFRP rod and each component of the joint under varying tensile loads are calculated using Eqs. (29)–(36). The results are illustrated in Fig. 15(a), where the horizontal axis represents the normalized tensile load. The results indicate that the FSM of HFRP rod body is consistently higher than that of all components of the joint under the same tensile load, suggesting that the carbon rod joint will fail first under identical loading conditions. Moreover the

fatigue limit load for the φ 22 mm HFRP rod is 0.57 F_{A-cr} (183.6 kN), while the fatigue limit load for its joint is 0.28 F_{A-cr} (91.5 kN). Fig. 15(b) and (c) depict the FSM of HFRP rod and each component of the joint under various bending moments and torques when subjected to a tensile load of 0.20 F_{A-cr} (64.2 kN). As shown in Fig. 15(b), the FSM of steel joint and resin adhesive decreases gradually with increasing torque. Conversely, FSM of the HFRP rod body and HFRP rod at the joint remains relatively stable initially but declines rapidly once the torque exceeds a certain threshold. Specifically, when the torque reaches 0.67 M_{T-cr} (89.3 N m), FSM of the HFRP rod at the joint drops to zero. Fig. 15(c) shows that with increasing bending moment, FSM of HFRP rod body decreases slowly, while FSM of each component at the joint decrease linearly,

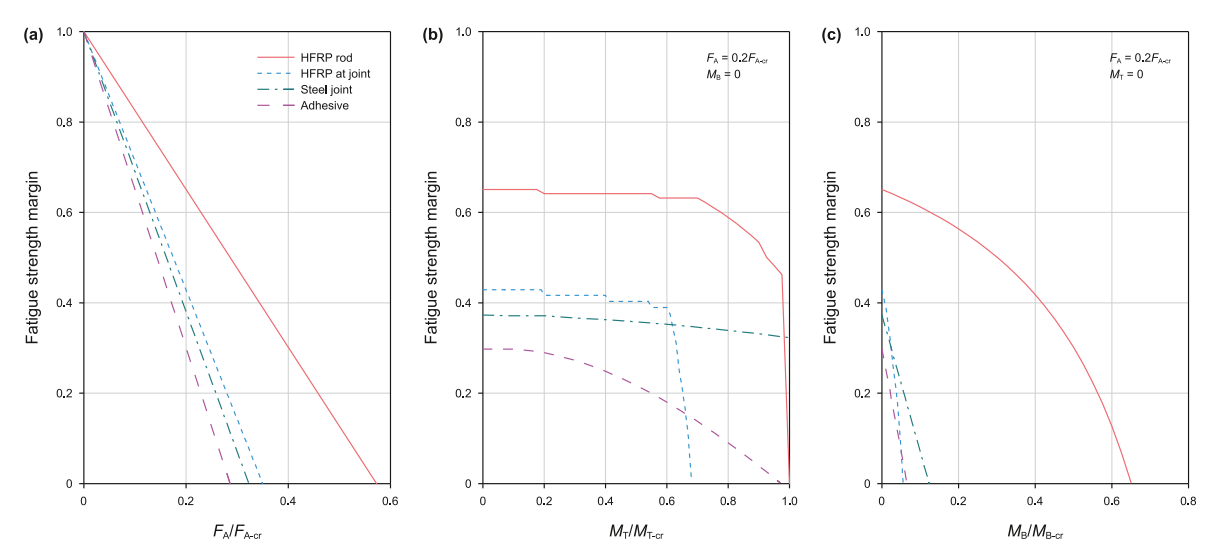


Fig. 15. Effect of load on FSM for HFRP rod and the joint. (a) Tensile load; (b)bending load; (c) torsion load.

with HFRP rod at the joint exhibiting the most rapid decline. When the bending moment reaches 0.06 M_{B-cr} (71.5 N m), FSM of the HFRP rod joint also falls to zero.

These findings indicate that, under a given tensile load, lower bending moments and torques can induce fatigue failure in the HFRP rod at the joint. Therefore, it is crucial to minimize the bending moments and torques experienced by the HFRP rod at joint in the design of SRS.

4.6. Prediction of complex load for SRS

Using a vertical well as a case study, the force dynamics of the SRS are analyzed, with the parameters of the oil production system detailed in Table 5. Fig. 16 illustrates all the loads borne by SRS.

As shown in Fig. 16(a), the axial load on the SRS decreases with increasing well depth. Due to the higher density of steel rods compared to HFRP rods, the reduction rate is more pronounced in steel rod sections. At the lower end of the SRS, the axial load becomes negative, triggering dynamic buckling within the SRS. As a result, the SRS incurs additional bending moments and torques. Fig. 16(b) and (c) clearly illustrate that both bending moment and torque exhibit significantly higher values at the lower end of SRS, gradually tapering off in an approximately exponential manner towards the top, where they approach zero. It is noteworthy that the maximum bending moment and torque do not occur at the very bottom of SRS but are shifted several tens of meters upwards due to the constraints imposed by the plunger inside the pump barrel. The maximum and minimum values of torque are relatively consistent, whereas the minimum bending moment is zero. Specifically, at the lower joint, the torque and bending moment stand at 1.1 N m and 23.2 N m, respectively. Despite their relatively small magnitudes, the sensitivity of the HFRP rod at joint to bending moments and torques leads to a significant reduction in tensile capacity, specifically to 0.51 F_{A-cr} . Compared with the upper joint that almost only bears axial load, its tensile capacity is reduced by 0.1 F_{A-cr} (34.0 kN)

According to Eqs. (13)–(15), the effect of the sinker bar diameter and well depth on the additional bending moment and torque experienced by SRS, with an inner tubing diameter of 62 mm, is analyzed. The results are illustrated in Fig. 17. As the diameter of the sinker bar increases, the critical load of helical buckling rises sharply. Additionally, as the well depth increases, the minimum diameter (d_h) required to prevent buckling of SRS also increases. For well depths of 1000 m, 2000 m, and 3000 m, the corresponding values of d_h are 19.1 mm, 31.8 mm, and 38.1 mm, respectively.

Fig. 17(b) demonstrates that, upon buckling of the rod string, a larger sinker bar diameter leads to a higher additional bending moment and a lower additional torque. To prevent damage to the HFRP rods caused by additional bending moments and torques, it is crucial to ensure that the SRS remains unbuckled. Furthermore, increasing the diameter of sinker bar will enhance the flow velocity of the well fluid, which in turn increases the viscous friction and energy consumption. Consequently, the diameter of sinker bar can be preferably $d_{\rm h}$.

5. Experimental verification

5.1. Verification of meso FEM

The accuracy of the meso FEM was validated by comparing the predicted fiber axial tensile strength (FATS) results of the unidirectional CFRP and GFRP with the experimental results.

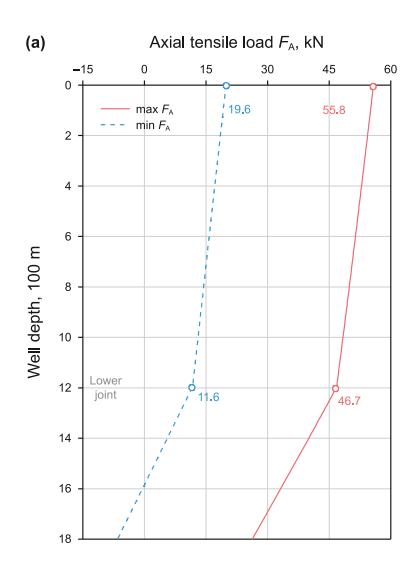
The FATS of the CFRP and GFRP used in HFRP sucker rods was tested under national standard of GB/T 1447–2005 (Fiber-reinforced plastics composites- Determination of tensile properties tensile properties). First, five rectangular tensile plates of CFRP and five rectangular tensile plates of GFRP were cut into specimens as shown in Fig. 18. Each specimen had a total length of 250 mm, a thickness *T* of 2 mm, a width *B* of 15 mm, and 50 mm anchoring length on each end. Then, the loading speed was set at 5 mm/min, and five tests were performed. The test results are depicted in

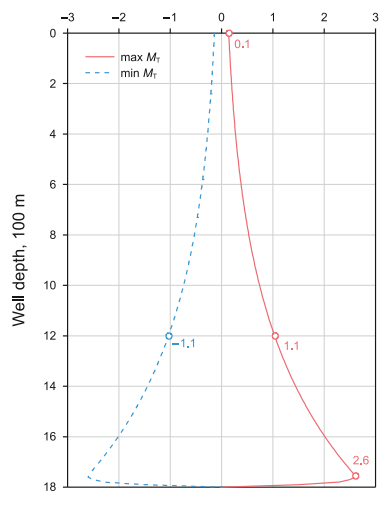
Table 5 Parameters of case well.

Parameters	Configuration of SRS			Configuration of tubing	Pump depth
value	HFRP rod φ 22 mm \times 1200	$0 \text{ m} + \text{steel rod } \phi 22 \text{ mm} \times 0$	600 m	ϕ 62/73 mm × 1800 m(Anchored)	1800 m
Parameters	submergence depth	pump diameter	Stroke length	Pumping speed	Water cut
value	400 m	56 mm	4.8 m	2/min	50%

Torsional load M_T, N·m

(b)





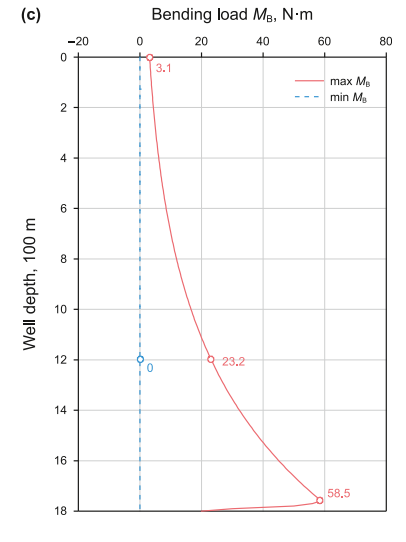


Fig. 16. Loads on the SRS of the case well.

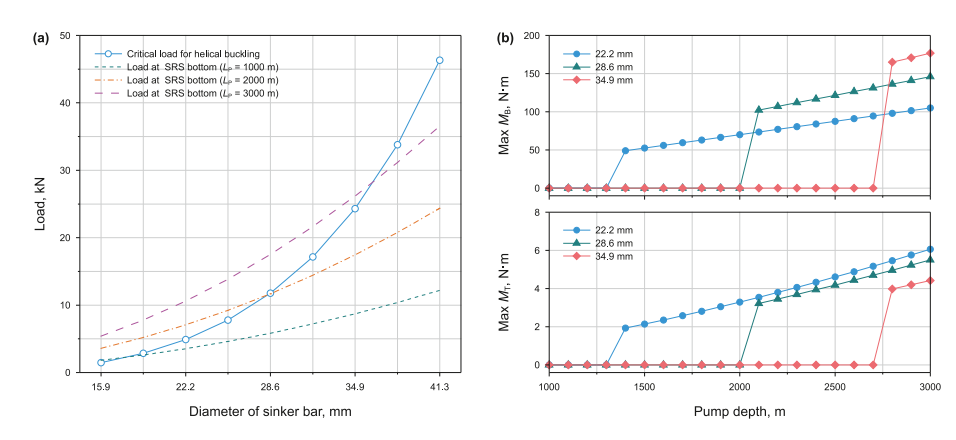


Fig. 17. Effect of sinker bar diameter and well depth on the additional bending moment and torque of the SRS. (a) critical load for helical buckling; (b) Effect of well depth on maximum additional bending moment and torque.

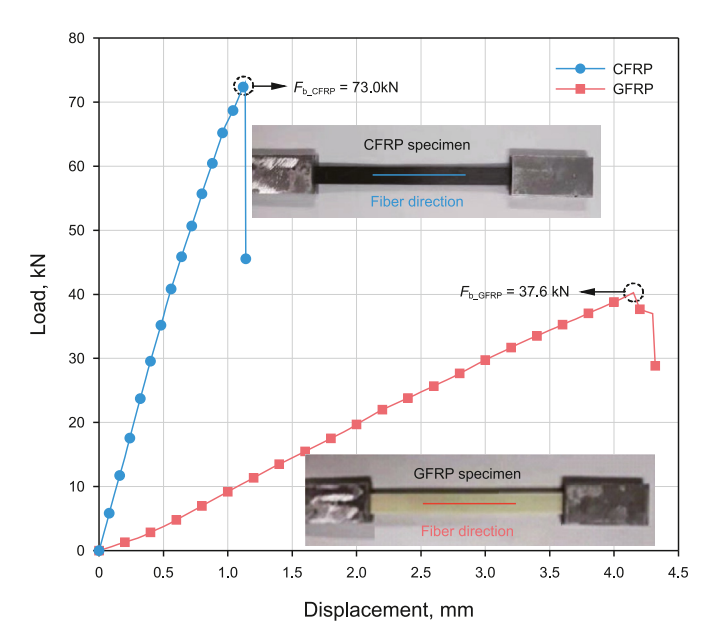


Fig. 18. Test result of FATS for unidirectional CFRP and GFRP.

Fig. 18, where the ultimate load indicated is the average of the five tests. Based on the formula $\sigma_b = F_b/(BT)$, the measured FATS of CFRP and GFRP were obtained and are presented in Table 6. The errors between the predicted and measured results were 6.2% and 4.4%, respectively, validating the precision of the meso FEM and the effectiveness of MMF.

5.2. Verification of dual-scale failure evaluation method

The effectiveness of the dual-scale failure assessment method was validated by comparing the predicted and tested critical tensile loads and bending moments of the φ 22 mm HFRP sucker rod.

The axial tensile strength of φ 22 mm HFRP rods was tested under national standard of GB/T 13096-2008 (Test method for

Table 6Comparison of predicted and measured FATS of CFRP and GFRP.

	Measured FATS, MPa	Predicted FATS, MPa	Error, %
CFRP	2434,2	2283.1	6.2
GFRP	1253.3	1197.6	4.4

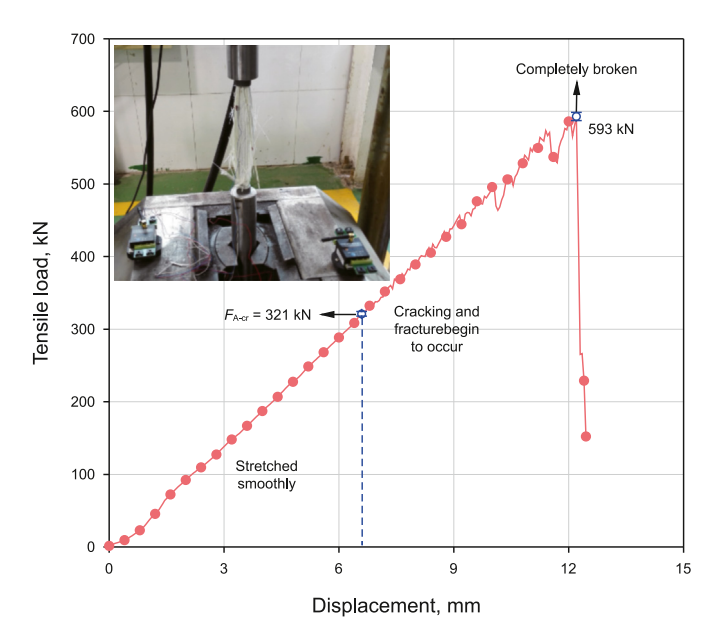


Fig. 19. Tensile test results of φ 22 mm HFRP rods.

mechanical properties of pultruded glass fiber reinforced plastic rods). Initially, five 700 mm-long HFRP rods were fabricated as specimens. The tensile test was conducted with a grip length of 65 mm and a loading speed of 5 mm/min. The test results are illustrated in Fig. 19, with the load values representing the average of five tests. Firstly, the HFRP rod specimens were stretched smoothly. When the tensile load reached 321 kN, the glass fibers on the rod's surface began to separate from the resin matrix and fracture. During this phase, the HFRP rod's stiffness remains relatively stable, with only a slight decline, maintaining the displacement-load curve's linear ascent. However, the load experienced fluctuations due to the release of elastic potential energy from the fracturing glass fibers, with the oscillation amplitude increasing as the displacement increased. Although the rod did not fracture completely until 593 kN (equivalent to a tensile ultimate strength of 1560 MPa), the resin and fibers began to fail at 321 kN, which was identified as the critical tensile load for the HFRP rod.

The bending properties of ϕ 22 mm HFRP rods were tested under national standard of GB/T 14028.2—2009 (Textile-glass-reinforced plastics - Determination of mechanical properties on rods made of roving-reinforced resin - Part 2: Determination of flexural strength). Five 440 mm-long HFRP rods were fabricated as

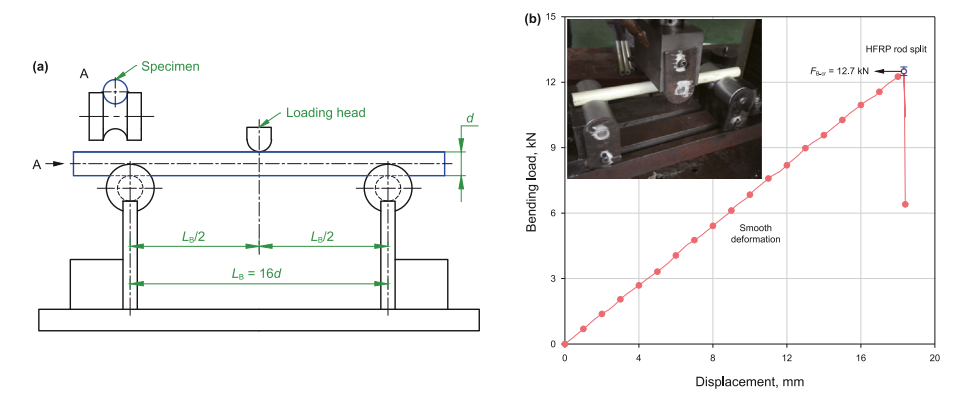


Fig. 20. Bending strength test of HFFP rod. (a) Diagram of the three-point bending test device; (b) Test results.

Table 7Comparison of Predicted and Measured Critical loads,

	Critical tensile load, kN	Critical bending moment, $N \cdot m$
Predicted	340.2	1192.4
Measured	321.0	1117.6
Error, %	6.0	6.7

specimens. The three-point bending experiment was conducted using a microcomputer controlled electronic universal testing machine (WDW-300E) with the schematic diagram shown in Fig. 20(a). The bending span $L_{\rm B}$ was set to be 16 times the rod diameter, which is 352 mm. The loading speed was set at 2 mm/min, and the test results are shown in Fig. 20(b), where the marked load $F_{\rm B-cr}=12.7$ kN represents the average from five tests. Using Eq. (39), the critical bending moment for the φ 22 mm HFRP rod was calculated to be 1117.6 N m.

$$M_{\mathrm{B-cr}} = F_{\mathrm{B-cr}} L_{\mathrm{B}} / 4 \tag{39}$$

Table 7 presents the predicted and tested results of the critical tensile load and bending moment of φ 22 mm HFRP rods. The errors of the two critical loads are 6.0% and 6.7%, respectively. The predicted values of critical tensile and bending loads are higher than the test values. This discrepancy arises because the macro-scale and meso-scale FEMs did not account for defects in the HFRP rod, such as uneven fiber arrangement (as shown in Fig. 4(a)) and the serrated edges of the carbon core layer (depicted in Fig. 1). In the

design of SRS, a safety factor of at least 1.25 is generally required, rendering the prediction error acceptable. These results demonstrate that the proposed dual-scale failure criterion can effectively assesses the failure of HFRP rods.

5.3. Verification of Equivalent fatigue failure evaluation method

Based on the simulation results presented in Section 3.5.1, the analysis identifies a total of six potential failure points—S1, S2, S3, S4, A1, and A2—and one hazardous cross section, H1, at the HFRP rod joint, as illustrated in Fig. 21. The FSM analysis of the joint components under complex loading conditions reveals that all these points and cross section have the potential to be destroyed first. Specifically, as shown in Fig. 21(a), if the points S1 through S4 on the rotary joint fail first, the cyclic loading could induce fatigue fractures at the joint. Alternatively, if the points A1 or A2, located on the resin adhesive, fail initially, the HFRP rod at these points may detach from the adhesive. This detachment will ultimately lead to complete separation of the HFRP rod from the joint due to adhesive debonding, as shown in Fig. 21(b).

As shown in Fig. 21(c), if the cross section H1 fails first, the GFRP winding layer will initially sustain damage under predominant tensile and bending loads, resulting in cracks that propagate in multiple directions. Once the GFRP coating layer is entirely compromised, the load will be borne solely by the interface between the GFRP coating layer and the CFRP core layer, specifically the GFRP winding layer. This scenario will result in the detachment of the CFRP core layer from the GFRP coating layer, ultimately

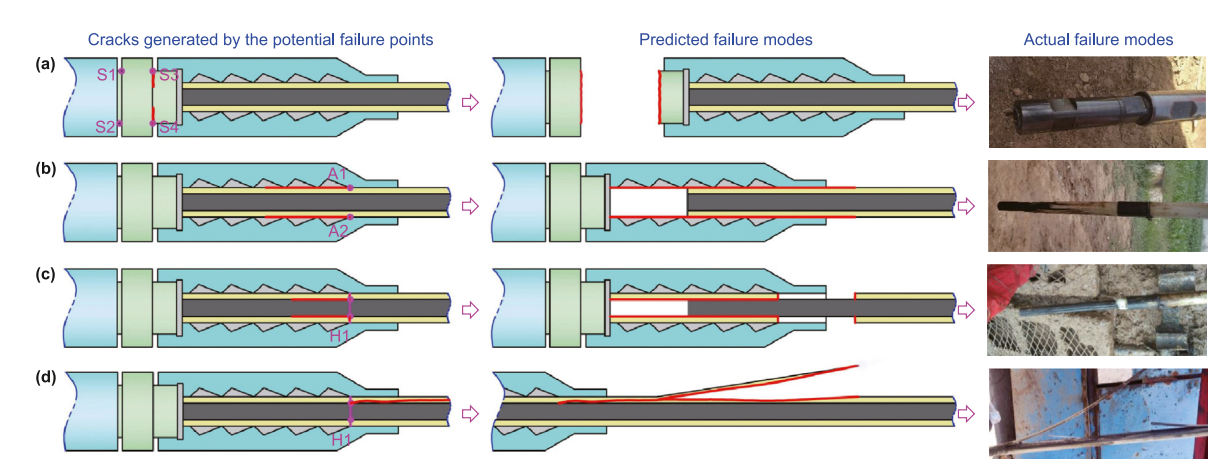


Fig. 21. Cause for various failures of HFRP rod joints. (a) Rotary joint fracture caused by destruction of points SI – S4; (b) Adhesive debonding caused by destruction of points Al and A2; (c) Interface debonding caused by destruction of cross-section HI:

Table 8Performance of the oil production systems designed by both conventional and concentrated weighting strategies.

Parameters	Conventional Weighting (Original)	Concentrated weighting (New)	Comparison, %
Diameter of HFRP, mm	22	22	0
Length of HFRP, m	1300	2400	84.6
Diameter of sinker bar, mm	22	38	72.7
Length of sinker bar, m	1500	400	-73.3
Pumping speed, /min	1.60	1.70	6.3
Production rate, m ³ /day	9.68	9.81	1.3
System efficiency, %	31.63	31.98	1.0
Max load at upper joint, kN	64.4	59.6	-7.4
Max load at lower joint, kN	55.1	42.8	-22.3
Min laod at lower SRS, kN	-10.3	-30.9	-200.0
Max M_B at upper joint, N·m	13.3	0	-100.0
Max M_B at lower joint, N·m	33.6	0	-100.0
Max M_T at upper joint, N·m	0.7	0	-100
Max M_T at lower joint, N·m	1.9	0	-100
Production cycle, day	67	512	664.2
Failure mode	Interface debonding in HFRP rod of the lower joint	No failure yet	_

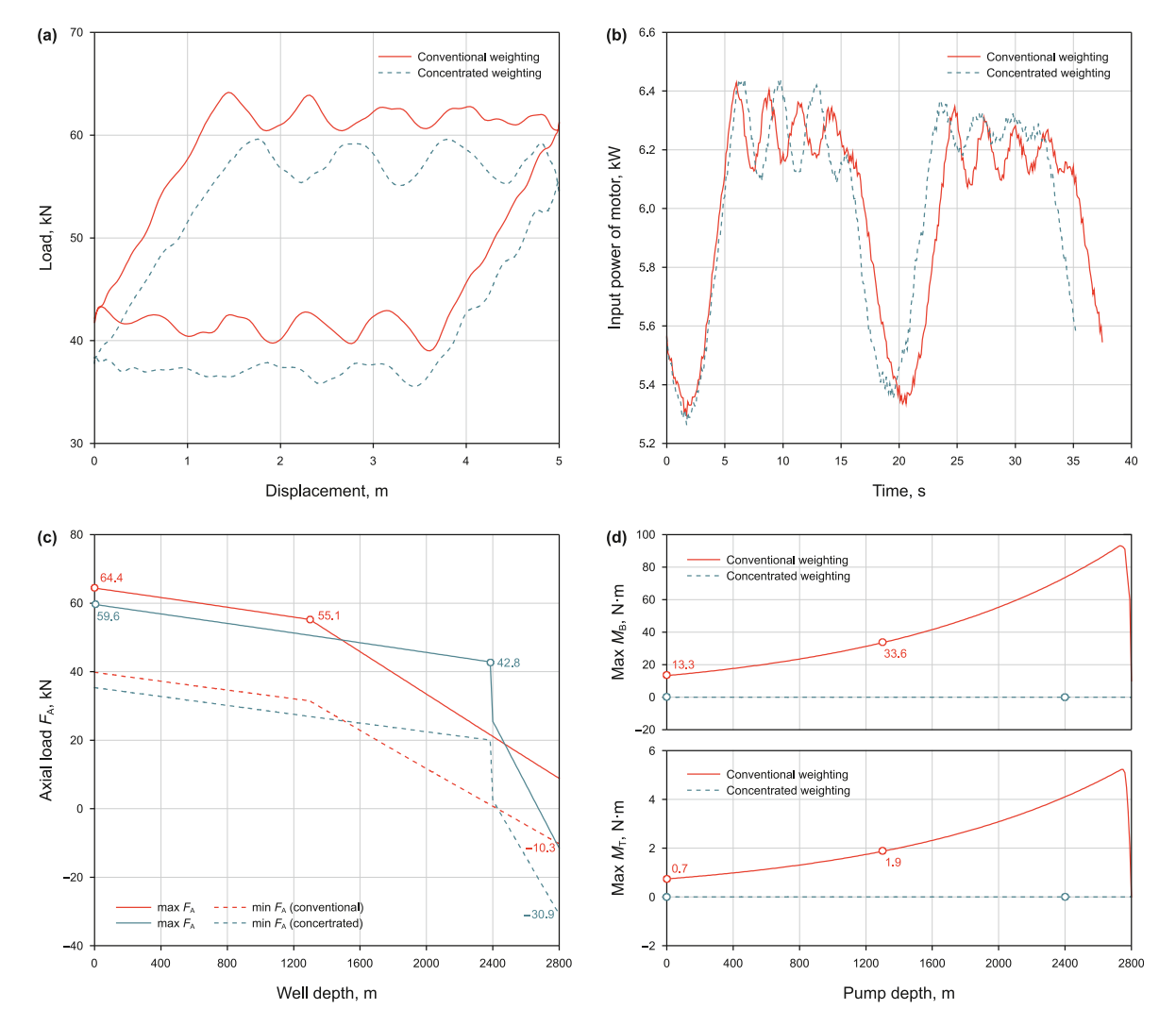


Fig. 22. Comparison of loads and FSM of SRS under conventional and concentrated weighting strategies. (a) Dynamometer cards; (b) Instantaneous input power of motor; (c) Axial loads; (d) Bending moments and torques.

leading to the separation of the HFRP rod from the joint due to interface debonding. Moreover, the propagation of cracks in the GFRP coating and winding layer along the axial direction outside the joint may induce cracking in the HFRP rod near the joint, as

depicted in Fig. 21(d). The actual failure mode of the HFRP rod joint in practical applications aligns with the FEM prediction results, thereby validating the accuracy and effectiveness of the finite element analysis for the HFRP rod joint.

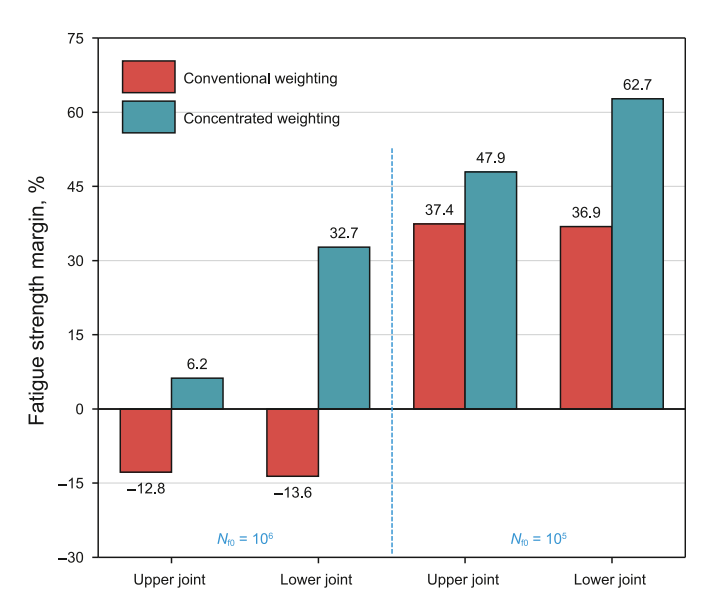


Fig. 23. FSM of upper and lower joints.

5.4. Solutions and field tests

From the above analysis, it can be concluded that the root cause for the observed multi-mode failures in the joint is the sensitivity of the joint and HFRP rod to the bending moment and torque caused by the SRS dynamic buckling. Additionally, the presence of multiple potential failure points within the joint due to stress concentration further exacerbates the failure modes. Based on this conclusion, a design strategy for a mixed SRS comprising HFRP and steel rods with concentrated weighting is proposed. This strategy involves employing rods with larger diameters and shorter lengths as sink bars. This approach ensures that the mixed SRS maintains structural stability against buckling while simultaneously increasing the proportion of HFRP rods, thus reducing the overall weight of SRS. The effectiveness of this proposed design strategy was validated through application in real-world oil wells. The main parameters of the oil well for this application are as follows: pump diameter of 38 mm, submergence depth of 1000 m, water content of 63.5%, allocated liquid production of 10 m³/day, pump hanging depth of 2800 m, belt pumping unit, stroke length of 5 m, Y280S-8 motor with a power rating of 37 kW, and an inner diameter of the tubing of 62 mm.

The performance of SRPS, designed by both conventional and concentrated weighting strategies, is detailed in Table 8, while the specific loads and FSP of SRS are illustrated in Figs. 22 and 23.

As detailed in Table 8, a steel rod with dimensions of 38 mm in diameter and 400 m in length was employed as the sinker bar, replacing the original weighting rod. The measured dynamometer cards for the two SRPS are illustrated in Fig. 22(a). In the new SRPS, the utilization of HFRP rods with a larger length results in reduced stiffness of SRS, which consequently decreases the effective stroke of the plunger. To maintain liquid production rate, the pumping speed was increased by 0.1/min, and the liquid production has slightly increased by 1.3%. Fig. 22(b) illustrates the measured instantaneous input power of the motor for the two SRPS. The instantaneous input power of the new system is slightly higher, but the cycle is shorter and the production rate is slightly higher, so the system efficiency remains basically unchanged.

As shown in Fig. 22(c), the axial loads in the new SRPS are lower across the entire HFRP rod compared to the original SRPS. Notably, the maximum axial load at the upper and lower joints have

decreased by 7.4% and 22.3%, respectively. Although the new SRPS experiences a 20.6 kN increase in maximum compressive load at the SRS bottom, this does not induce extra bending moments or torques, as it remains below the critical buckling load of the sinker bar. Fig. 22(d) highlights the additional bending moments and torques in the original SRPS, peaking at 13.3 N m and 0.7 N m at the upper joint, and 33.6 N m and 1.9 N m at the lower joint, respectively. In contrast, the new SRPS incurs no such additional stresses.

Based on the SRS loads, the FSM for both the upper and lower joints is derived, as depicted in Fig. 23. For $N_{\rm f0}=10^6$, the FSM values for both joints in the new SRPS remain positive, whereas the original SRPS exhibits negative FSM values, particularly for the lower joint, aligning with the observed debonding at the lower joint's HFRP rod. The new SRPS can sustain SRS force cycles exceeding 10^6 , equivalent to 408.5 days given the pumping speed, congruent with its current operational period of 512 days without failure. At $N_{\rm f0}=10^5$, both joints in the original SRPS exhibit positive FSM, indicating a fatigue life potentially exceeding 10^5 cycles (43.4 days), consistent with its 67-day safe production record. These observations validate the proposed equivalent fatigue assessment method. Furthermore, the new SRPS's safe production time extends 664.2% longer than that of the original SRPS, underscoring the efficacy of the proposed strategy.

6. Conclusions

To enhance the reliability of HFRP rods and their joints, this study introduces a dual-scale failure evaluation method for HFRP rods and an equivalent fatigue failure assessment method for HFRP rod joints. These methodologies enable a thorough analysis of the mechanical characteristics and failure modes of HFRP components under complex loading conditions, thereby providing a deeper understanding of their performance. Key findings reveal that: (1) Stress concentration at the joint significantly reduces the tensile, bending, and torsional strengths of HFRP rods to 61%, 12%, and 82% of their original capacities, respectively. (2) Bending moments linearly diminish the tensile capacity of HFRP rods, while torque initially causes a slight reduction before leading to a sharp decline in tensile strength. (3) The primary cause of joint failure is the susceptibility of both the joint and the HFRP rod to bending moments and torque induced by dynamic buckling of SRS. Leveraging these insights, the study proposes a novel design method for HFRPsteel mixed rods with concentrated weighting, aimed at substantially enhancing the service life and reliability of SRS structures. Field tests and indoor experiments unequivocally showcase the practical applicability of the proposed method, underscoring its potential to substantially enhance the durability of HFRP rods and their joints. These findings not only address the critical need for understanding HFRP rod joint failures but also provides an effective method for evaluating and designing composite materials with superior performance.

CRediT authorship contribution statement

Xiao-Xiao Lv: Writing — review & editing, Writing — original draft, Validation, Software, Methodology, Investigation. **Wen-Rui Jin:** Supervision, Resources, Conceptualization. **Xin Zhang:** Investigation, Funding acquisition, Data curation.

Declaration of interest

No conflict of interest exits in the submission of this manuscript, and manuscript is approved by all authors for publication. I would like to declare on behalf of my co-authors that the work described was original research that has not been published previously, and

not under consideration for publication elsewhere, in whole or in part. All the authors listed have approved the manuscript that is enclosed.

Acknowledgment

The authors gratefully acknowledge financial support by the Fundamental Research Funds for the Central Universities under Grant no. 24CX02019A, the Opening Fund of National Engineering Research Center of Marine Geophysical Prospecting and Exploration and Development Equipment under Grant no. 24CX02019A.

Appendix

The off-axis stress transformation matrix is

$$\boldsymbol{T}_{\beta} = \begin{bmatrix} 0 & S_{\beta}^2 & C_{\beta}^2 & 2S_{\beta}C_{\beta} & 0 & 0 \\ 0 & C_{\beta}^2 & S_{\beta}^2 & -2S_{\beta}C_{\beta} & 0 & 0 \\ 1 & 0 & 0 & 0 & 0 & 0 \\ 0 & 0 & 0 & 0 & S_{\beta} & -C_{\beta} \\ 0 & 0 & 0 & 0 & C_{\beta} & S_{\beta} \\ 0 & -S_{\beta}C_{\beta} & S_{\beta}C_{\beta} & S_{\beta}^2 - C_{\beta}^2 & 0 & 0 \end{bmatrix}$$

where, $C_{\beta} = \cos \beta$; $S_{\beta} = \sin \beta$.

The stress conversion matrix between rectangular CS and cylindrical CS is

$$\mathbf{T}_{\text{CR}} = \begin{vmatrix} 0 & 0 & 1 & 0 & 0 & 0 \\ S_{\theta}^{2} & C_{\theta}^{2} & 0 & 0 & 0 & 2S_{\theta}C_{\theta} \\ C_{\theta}^{2} & S_{\theta}^{2} & 0 & 0 & 0 & -2S_{\theta}C_{\theta} \\ -S_{\theta}C_{\theta} & S_{\theta}C_{\theta} & 0 & 0 & 0 & C_{\theta}^{2} - S_{\theta}^{2} \\ 0 & 0 & 0 & C_{\theta} & S_{\theta} & 0 \\ 0 & 0 & 0 & -S_{\theta} & C_{\theta} & 0 \end{vmatrix}$$

$$\theta = \begin{cases} 0 & k \le 8 \\ 180^{\circ} & k > 8 \end{cases}$$

where θ is the polar angle of macro critical points; k is No. of macro critical points.

The stress transformation matrix corresponding to a rotation of the CS around the Y-axis by angle β is

$$\boldsymbol{T}_{y\beta} = \begin{bmatrix} C_{\beta}^2 & 0 & S_{\beta}^2 & 0 & -2S_{\beta}C_{\beta} & 0 \\ 0 & 1 & 0 & 0 & 0 & 0 \\ S_{\beta}^2 & 0 & C_{\beta}^2 & 0 & 2S_{\beta}C_{\beta} & 0 \\ 0 & 0 & 0 & C_{\beta} & 0 & S_{\beta} \\ S_{\beta}C_{\beta} & 0 & -S_{\beta}C_{\beta} & 0 & C_{\beta}^2 - S_{\beta}^2 & 0 \\ 0 & 0 & 0 & -S_{\beta} & 0 & C_{\beta} \end{bmatrix}$$

The stress coordinate transformation matrix when rotating around axis 1 is

$$\boldsymbol{T}_{1\psi} = \begin{bmatrix} 1 & 0 & 0 & 0 & 0 & 0 \\ 0 & C_{\psi}^2 & S_{\psi}^2 & 0 & 0 & -2S_{\psi}C_{\psi} \\ 0 & S_{\psi}^2 & C_{\psi}^2 & 0 & 0 & 2S_{\psi}C_{\psi} \\ 0 & 0 & 0 & C_{\psi} & -S_{\psi} & 0 \\ 0 & 0 & 0 & S_{\psi} & C_{\psi} & 0 \\ 0 & S_{\psi}C_{\psi} & -S_{\psi}C_{\psi} & 0 & 0 & C_{\psi}^2 - S_{\psi}^2 \end{bmatrix}$$

References

- Cao, Miao., Gao, X., Tang, B., Dai, Z., Li, H., Yi, J., 2023. Multiscale thermal oxidative ageing mechanisms of carbon fiber/epoxy plain woven composites under short beam shear loading. Thin-Walled Struct. 185, 110566. https://doi.org/10.1016/j. tws.2023.110566.
- Chang, F.K., Chang, K.Y., 1987. A progressive damage model for laminated composites containing stress concentrations. J. Compos. Mater. 21, 834–855. https://doi.org/10.1177/002199838702100904.
- Cheng, T.C., Jiang, M.Z., Dong, K.X., Li, W., Bao, Z.S., Zhang, Q., 2021. Post-buckling analysis of two-layer contact concentric tubular strings in pipe. J. Pet. Sci. Eng. 207, 109272. https://doi.org/10.1016/j.petrol.2021.109272.
- Cózar, I.R., Otero, F., Maimí, P., González, E.V., Turon, A., Camanho, P.P., 2024. An enhanced constitutive model to predict plastic deformation and multiple failure mechanisms in fibre-reinforced polymer composite materials. Compos. Struct. 330, 117696. https://doi.org/10.1016/j.compstruct.2023.117696.
- Elgaddafi, R., Ahmed, R., Shah, S., 2021. The effect of fluid flow on CO2 corrosion of high-strength API carbon steels. J. Nat. Gas Sci. Eng. 86, 1–14. https://doi.org/10.1016/j.jngse.2020.103739.
- Feng, Y.Q., Hao, H.L., Chow, C.L., Lau, D., 2024. Exploring reaction mechanisms and kinetics of cellulose combustion via ReaxFF molecular dynamics simulations. Chem. Eng. J. 488, 151023. https://doi.org/10.1016/j.cej.2024.151023.
- Gu, J.F., Chen, P.H., 2017. Some modifications of Hashin's failure criteria for unidirectional composite materials. Compos. Struct. 182, 143–152. https://doi.org/10.1016/j.compstruct.2017.09.011.
- Guo, R., Xian, G.J., Li, C.G., Hong, B., 2022a. Effect of fiber hybrid mode on the tension – tension fatigue performance for the pultruded carbon/glass fiber reinforced polymer composite rod. Eng. Fract. Mech. 260, 108208. https://doi.org/10.1016/ j.engfracmech.2021.108208.
- Guo, R., Xian, G.J., Li, C.G., Hong, B., Huang, X.Y., Xin, M.Y., Huang, S.D., 2021. Water uptake and interfacial shear strength of carbon/glass fiber hybrid composite rods under hygrothermal environments: effects of hybrid modes. Polym. Degrad. Stabil. 193, 109723. https://doi.org/10.1016/j.jpolymdegradstab.2021.109723.
- Guo, R., Xian, G.J., Li, C.G., Huang, X.Y., Xin, M.Y., 2022b. Effect of fiber hybridization types on the mechanical properties of carbon/glass fiber reinforced polymer composite rod. Mech. Adv. Mater. Struct. 29, 6288–6300. https://doi.org/ 10.1080/15376494.2021.1974620.
- Guo, R., Xian, G.J., Li, F., Li, C.G., Hong, B., 2022c. Hygrothermal resistance of pultruded carbon, glass and carbon/glass hybrid fiber reinforced epoxy composites. Constr. Build. Mater. 315, 125710. https://doi.org/10.1016/j.conbuildmat.2021.125710.
- Ha, S.K., Huang, Y., Han, H.H., Jin, K.K., 2010. Micromechanics of failure for ultimate strength predictions of composite laminates. J. Compos. Mater. 44 (20), 2347–2361. https://doi.org/10.1177/0021998310372464.
- Hafiz, T.A., Abdel-Wahab, M.M., Crocombe, A.D., Smith, P.A., 2013. Mixed-mode fatigue crack growth in FM73 bonded joint. Int. J. Adhesion Adhes. 40 (3), 188e196. https://doi.org/10.1016/j.ijadhadh.2012.07.004.
- Hasheminia, S.M., Park, B.C., Chun, H.J., Park, J.C., Chang, H.S., 2019. Failure mechanism of bonded joints with similar and dissimilar material. Compos. B Eng. 161, 702e709. https://doi.org/10.1016/j.compositesb.2018.11.016.
- Hashin, Z., 1987. Comments on the fatigue failure criterion of the mixed model. Eng. Fract. Mech. 26, 157. https://doi.org/10.1016/0013-7944(87)90087-7.
- Hou, Y.L., Wang, W.H., Meng, L., Sapanathan, T., Li, J.S., Xu, Y.J., 2022. An insight into the mechanical behavior of adhesively bonded plain-woven-composite joints using multiscale modeling. Int. J. Mech. Sci. 219, 107063. https://doi.org/ 10.1016/j.ijmecsci.2022.107063.
- Ji, Z.S., Niu, D.X., Li, W.Y., Wu, G.Q., Yang, X.L., Sun, L.J., 2022. Improving the energy efficiency of China: an analysis considering clean energy and fossil energy resources. Energy 259, 124950. https://doi.org/10.1016/j.energy.2022.124950
- sources. Energy 259, 124950. https://doi.org/10.1016/j.energy.2022.124950. Jiang, J.X., Wan, X.L., Li, K.J., Du, J.G., Liu, Y.H., Jing, J.J., Li, J.S., 2024. Research progress of sucker rod fracture detection and prediction model. Eng. Fail. Anal. https://doi.org/10.1016/j.engfailanal.2024.108119.
- Ke, L., Zhang, R.D., Feng, Z., Li, C.X., Li, Y.L., 2024. Performance evolution of epoxy adhesive and CFRP-steel epoxy-bonded joints subjected to hygrothermal

exposure. Constr. Build. Mater. 429. https://doi.org/10.1016/j.conbuildmat.2024.136445.

- Kim, K.S., Yi, Y.M., Cho, G.R., Kim, C.G., 2008. Failure prediction and strength improvement of uni-directional composite single lap bonded joints. Compos. Struct. 82 (4), 513e520. https://doi.org/10.1016/j.compstruct.2007.02.005.
- Lei, Q., Xu, Y., Yang, Z.W., Cai, B., Wang, X., Zhou, L., Liu, H.F., Xu, M.J., Wang, L.W., Li, S., 2021. Progress and development directions of stimulation techniques for ultra-deep oil and gas reservoirs. Petrol. Explor. Dev. 48, 193–201. https:// doi.org/10.11698/PED.2021.01.18.
- Li, C.G., Guo, R., Xian, G.J., Li, H., 2020a. Effects of elevated temperature, hydraulic pressure and fatigue loading on the property evolution of a carbon/glass fiber hybrid rod. Polym. Test. 90, 106761. https://doi.org/10.1016/j.polymertesting.2020.106761.
- Li, C.G., Guo, R., Xian, G.J., Li, H., 2020b. Innovative compound-type anchorage system for a large-diameter pultruded carbon/glass hybrid rod for bridge cable. Mater. Struct. Constr. 53. https://doi.org/10.1617/s11527-020-01510-v.
- Li, C.G., Xian, G.J., Li, H., 2018. Influence of immersion in water under hydraulic pressure on the interfacial shear strength of a unidirectional carbon/glass hybrid rod. Polym. Test. 72, 164–171. https://doi.org/10.1016/j.polymertesting.2018.10.004.
- Li, C.G., Xian, G.J., Li, H., 2019a. Tension-tension fatigue performance of a large-diameter pultruded carbon/glass hybrid rod. Int. J. Fatig. 120, 141–149. https://doi.org/10.1016/j.ijfatigue.2018.11.007.
- Li, C.G., Xian, G.J., Li, H., 2019b. Combined effects of temperature, hydraulic pressure and salty concentration on the water uptake and mechanical properties of a carbon/glass fibers hybrid rod in salty solutions. Polym. Test. 76, 19–32. https://doi.org/10.1016/j.polymertesting.2019.02.034.
- Li, C.G., Yin, X.L., Liu, Y.C., Guo, R., Xian, G.J., 2020c. Long-term service evaluation of a pultruded carbon/glass hybrid rod exposed to elevated temperature, hydraulic pressure and fatigue load coupling. Int. J. Fatig. 134. https://doi.org/10.1016/ i.i/fatigue.2020.105480.
- Li, C.G., Yin, X.L., Wang, Y.J., Zhang, L., Zhang, Z.H., Liu, Y.C., Xian, G.J., 2020d. Mechanical property evolution and service life prediction of pultruded carbon/glass hybrid rod exposed in harsh oil-well condition. Compos. Struct. 246. https://doi.org/10.1016/j.compstruct.2020.112418.
- Li, X., Gao, Q., Cao, Y.Y., Yang, Y.F., Liu, S.M., Wang, Z.L., Cheng, T.H., 2022. Optimization strategy of wind energy harvesting via triboelectric-electromagnetic flexible cooperation. Appl. Energy 307. https://doi.org/10.1016/j.apenergy.2021.118311.
- Li, X., Guan, Z.D., Liu, L., Li, Z.S., 2013. Composite multiscale failure criteria and damage evolution. Acta Mater. Compos. Sin. 30 (2), 152–158. https://doi.org/ 10.13801/j.cnki.fhclxb.2013.02.003 (in Chinese).
- Liu, Y.H., Huang, K., Wang, Z.X., Li, Z.G., Chen, L.L., Shi, Q.Z., Yu, S.Y., Li, Z.X., Zhang, L., Guo, L.C., 2023. Cross-scale data-based damage identification of CFRP laminates using acoustic emission and deep learning. Eng. Fract. Mech. 294, 109724. https://doi.org/10.1016/j.engfracmech.2023.109724.
- Lv, X.X., Jin, W.R., Zhang, T., Wang, H.X., 2023. Multi-objective holistic optimization method for CR SRPS based on cross-scale failure simulation of composite to improve oil recovery benefits. Geoenergy Sci. Eng. 227, 211878. https://doi.org/ 10.1016/j.geoen.2023.211878.
- Lv, X.X., Wang, H.X., Zhang, X., Liu, Y.X., Chen, S.S., 2021. An equivalent vibration model for optimization design of carbon/glass hybrid fiber sucker rod pumping system. J. Pet. Sci. Eng. 207. https://doi.org/10.1016/j.petrol.2021.109148.
- Meng, J., Hu, X.P., Chen, P.P., Coffman, D.M., Han, M.Y., 2020. The unequal contribution to global energy consumption along the supply chain. J. Environ. Manag. 268. https://doi.org/10.1016/j.jenvman.2020.110701.
- Mushtaq, S.F., Ali, A., Khushnood, R.A., Tufail, R.F., Majdi, A., Nawaz, A., Durdyev, S., Burduhos Nergis, D.D., Ahmad, J., 2022. Effect of bentonite as partial replacement of cement on residual properties of concrete exposed to elevated temperatures. Sustain. Times 14. https://doi.org/10.3390/su141811580.
- Noh, H.K., Go, M.S., Lim, J.H., Choi, Y.H., Kim, J.G., 2023. Numerical modeling and experimental validation of lamina fracture and progressive delamination in composite dovetail specimens under tensile loading. Compos. Struct. 325, 117578, https://doi.org/10.1016/j.compstruct.2023.117578.
- Ozel, A., Yazici, B., Akpinar, S., Aydin, M., Temiz, S., 2014. A study on the strength of adhesively bonded joints with different adherends. Compos. B Eng. 62, 167e174. https://doi.org/10.1016/j.compositesb.2014.03.001.
- Qi, Z.C., Liu, Y., Chen, W.L., 2019. An approach to predict the mechanical properties of CFRP based on cross-scale simulation. Compos. Struct. 210, 339—347. https:// doi.org/10.1016/j.compstruct.2018.11.056.
- Reis, P.N.B., Ferreira, J.A.M., Antunes, F., 2011. Effect of adherend's rigidity on the shear strength of single lap adhesive joints. Int. J. Adhesion Adhes. 31 (4), 193–201. https://doi.org/10.1016/j.ijadhadh.2010.12.003.
- Rodsin, K., Joyklad, P., Hussain, Q., Mohamad, H., Buatik, A., Zhou, M., Chaiyasarn, K., Nawaz, A., Mehmood, T., Elnemr, A., 2022. Behavior of steel clamp confined brick aggregate concrete circular columns subjected to axial compression. Case Stud. Constr. Mater. 16, e00815. https://doi.org/10.1016/j.cscm.2021.e00815.
- Shi, S.L., Zhu, T.Q., Yan, W.D., Jian, X.G., Shen, L.L., Xu, J., 2024. Damage mechanism of interlayer interface of continuous carbon fiber-reinforced polyphthalazine ether

- sulfone ketone resin matrix composites: multi-scale study method at extreme temperature. Chem. Eng. J. 496, 153860. https://doi.org/10.1016/j.cei.2024.153860.
- Sun, X.R., Dong, S.M., Liu, M.S., Zhang, J.J., 2018. The simulation model of sucker rod string transverse vibration under the space buckling deformation excitation and rod-tubing eccentric wear in vertical wells. J. Vibroeng. 20, 283–299. https://doi.org/10.21595/jve.2017.19138.
- Tanulia, V., Wang, J., Pearce, G., Baker, A., Chang, P., Gangadhara Prusty, B., 2022. Experimental and computational assessment of disbond growth and fatigue life of bonded joints and patch repairs for primary airframe structures. Int. J. Fatig. 159, 106776. https://doi.org/10.1016/i.iifatigue.2022.106776.
- Tsai, S.W., Wu, E.M., 1971. A general theory of strength for anisotropic materials. J. Compos. Mater. 5 (1), 58–80. https://doi.org/10.1177/002199837100500106.
- van Dongen, B., van Oostrum, A., Zarouchas, D., 2018. A blended continuum damage and fracture mechanics method for progressive damage analysis of composite structures using XFEM. Compos. Struct. 184, 512–522. https://doi.org/10.1016/ i.compstruct.2017.10.007.
- Wang, H.B., Dong, S.M., 2021. Research on the coupled axial-transverse nonlinear vibration of sucker rod string in deviated wells. J. Vib. Eng. Technol. 9, 115–129. https://doi.org/10.1007/s42417-020-00214-5.
- Wang, H.B., Sun, X.R., Li, F.X., Li, W.C., Xin, S., Wang, C.L., Li, D.F., 2024. Simulation study on the longitudinal and transverse torsional coupling vibrations of directional well sucker rod strings. J. Vib. Eng. 1–14. http://kns.cnki.net/kcms/ detail/32.1349.tb.20240415.2254.006.html (in Chinese).
- Wang, Z., Li, C.G., Sui, L.L., Xian, G.J., 2021. Effects of adhesive property and thickness on the bond performance between carbon fiber reinforced polymer laminate and steel. Thin-Walled Struct. 158, 107176. https://doi.org/10.1016/ i.tws.2020.107176.
- Wang, Z., Xian, G.J., 2021. Effects of thermal expansion coefficients discrepancy on the CFRP and steel bonding. Constr. Build. Mater. 269, 121356. https://doi.org/ 10.1016/j.conbuildmat.2020.121356.
- Wu, G.H., Li, D.Y., Lai, W.J., Shi, Y.D., Kang, H., Peng, Y.H., Su, X.M., 2021. Fatigue behaviors and mechanism-based life evaluation on SPR-bonded aluminum joint. Int. J. Fatig. 142, 105948. https://doi.org/10.1016/j.ijfatigue.2020.105948.
- Xian, G.J., Bai, Y.B., Zhou, P., Wang, J.Q., Li, C.G., Dong, S.C., Guo, R., Tian, J.W., Li, J.H., Zhong, J., He, T.P., Zhang, Z., 2024. Long-term properties evolution and life prediction of glass fiber reinforced thermoplastic bending bars exposed in concrete alkaline environment. J. Build. Eng. 91, 109641. https://doi.org/10.1016/j.jobe.2024.109641.
- Xian, G.J., Guo, R., Li, C.G., 2022. Combined effects of sustained bending loading, water immersion and fiber hybrid mode on the mechanical properties of carbon/glass fiber reinforced polymer composite. Compos. Struct. 281, 115060. https://doi.org/10.1016/j.compstruct.2021.115060.
- Xian, G.J., Guo, R., Li, C.G., Hong, B., 2021. Effects of rod size and fiber hybrid mode on the interface shear strength of carbon/glass fiber composite rods exposed to freezing-thawing and outdoor environments. J. Mater. Res. Technol. 14, 2812–2831. https://doi.org/10.1016/j.jmrt.2021.08.088.
- Yuan, K., Liu, K., Zhao, M.Q., Wei, K., Wang, Z.G., 2022. The in situ matrix cracking behavior in cross-ply laminates under out-of-plane shear loading. Compos. Struct. 290, 115563. https://doi.org/10.1016/j.compstruct.2022.115563.
- Zhang, H., Zhang, H.R., Zhang, X.Q., Sun, T., Liang, M., Chen, Y., Heng, Z.G., Zou, H.W., 2023b. In-situ self-assembled block copolymer nanowires on high-modulus carbon fibers surface for enhanced interfacial performance of CFRPs. Chem. Eng. J. 451, 138583. https://doi.org/10.1016/j.cej.2022.138583.
- Zhang, J., Li, H., Li, H.Y., 2022. Evaluation of multiaxial fatigue life prediction approach for adhesively bonded hollow cylinder butt-joints. Int. J. Fatig. 156, 106692. https://doi.org/10.1016/j.ijfatigue.2021.106692.
- Zhang, J.T., Yang, T., Du, Y., He, R.Y., Liu, C., 2024c. Tensile mechanical properties and damage analysis of layered woven GFRP composite bolts. Compos. Part B Eng. 271. https://doi.org/10.1016/j.compositesb.2023.111155.
- Zhang, K., Liu, X.F., Wang, D.B., Zheng, B., Chen, T.H., Wang, Q., Bai, H., Yao, E.D., Zhou, F.J., 2024a. A review of reservoir damage during hydraulic fracturing of deep and ultra-deep reservoirs. Pet. Sci. 21, 384–409. https://doi.org/10.1016/ j.petsci.2023.11.017.
- Zhang, Y.W., Che, J.Q., Pei, D.D., Wang, H.X., Zhang, J., Li, F., 2024c. Mechanics behavior and failure mechanism of the intralayer carbon/glass hybrid rod. Polym. Compos. 45, 7586–7601. https://doi.org/10.1002/pc.28290.
- Zhang, Y.W., Che, J.Q., Zhang, H., Li, F., Zhang, J., Wang, H.X., Pei, D.D., 2024b. An evaluation of the influence of mechanical strength on carbon/glass hybrid rods under various design parameters. Geoenergy Sci. Eng. 240. https://doi.org/10.1016/j.geoen.2024.212927.
- Zhang, Y.M., Xiao, Z.M., Zhang, W.G., Huang, Z.H., 2014. Strain-based CTOD estimation formulations for fracture assessment of offshore pipelines subjected to large plastic deformation. Ocean. Eng. 91, 64–72. https://doi.org/10.1016/j.oceaneng.2014.08.020.
- Zhang, Y.W., Che, J.Q., Wang, H.X., Zhang, J., Li, F., Du, M.C., Wang, Y.T., 2023a. Mechanical characteristic and failure mechanism of joint with composite sucker rod. Pet. Sci. 20, 3172–3183. https://doi.org/10.1016/j.petsci.2023.03.022.